Lithos 323 (2018) 156–173

Contents lists available at ScienceDirect

Lithos

journal homepage: www.elsevier.com/locate/lithos

Invited review article

In-situ oxygen isotope analyses in serpentine minerals: Constraints on serpentinization during tectonic exhumation at slow- and ultraslow-spreading ridges

Stéphane Rouméjon [a,*], Morgan J. Williams [b], Gretchen L. Früh-Green [a]

[a] Institute of Geochemistry and Petrology, ETH Zürich, Zürich CH-8092, Switzerland
[b] Research School of Earth Sciences, ANU Canberra, Acton 2601, Australia

ARTICLE INFO

Article history:
Received 5 March 2018
Revised 31 August 2018
Accepted 17 September 2018
Available online 22 September 2018

Keywords:
Oxygen isotopes
Serpentinization
Fluid-rock interaction
Atlantis Massif
Southwest Indian Ridge

ABSTRACT

Peridotites exhumed along detachment faults at slow- and ultraslow-spreading ridges undergo variable and complex serpentinization. Here, we present in-situ oxygen isotope analyses in serpentine minerals from a textural sequence identified in samples drilled at the Atlantis Massif (Mid-Atlantic ridge, MAR, 30°N) and dredged along the easternmost Southwest Indian ridge (SWIR, 62–65°E). The textural sequence is similar at both locations and involves: mesh texture and bastite formation after olivine and orthopyroxene, mesh texture recrystallization into chrysotile- and antigorite-dominated textures, and banded and fibrous veins. The $\delta^{18}O$ in serpentine decreases with the textural sequence, which we interpret to record an increase in the time-integrated water-rock ratio under a nearly constant temperature. While mesh texture development starts at stoichiometric water-rock ratios and creates an isotopic variability at a scale of ~100 μm, recrystallized textures indicate serpentinization temperatures on the order of 260–290 °C (seawater-dominated fluid hypothesis) or 320–360 °C (hydrothermally altered seawater hypothesis). The subsequent banded veins record the evolution towards colder and seawater-dominated fluids potentially present in shallower levels of the detachment footwall. Serpentinization leading to the mesh textures appears faster and more heterogeneous in Atlantis Massif samples than in SWIR samples. We propose that such features are influenced by the amount of gabbros intruded in the peridotite. In addition to influencing fluid pathways, gabbros also provide a source for observed Si-enrichments in some Atlantis Massif samples and control the pH, which in turn influences the mobility of Al.

1. Introduction

Exhumation and serpentinization of upper mantle peridotites is common along slow- and ultraslow-spreading ridges (full spreading rates <40 and < 20 mm yr^{-1}, respectively). In these settings, ultramafic rocks, intruded by variable amounts of gabbros, form the footwall of detachment fault zones (large offset normal faults; e.g., Cann et al., 1997) that bring fresh rocks in contact with seawater-derived hydrothermal fluids, leading to hydration and alteration. These systems have been recognized along the Mid-Atlantic Ridge (MAR; Karson et al., 1987; Cannat, 1993; Kelemen et al., 2004; Früh-Green et al., 2017; Früh-Green et al., 2018), the Southwest Indian Ridge (SWIR; Dick et al., 2003; Sauter et al., 2013), and the Arctic ridges (Michael et al., 2003). However, because direct observation of the reaction zone remains impossible, uncertainties still exist on how and under which conditions serpentinization occurs, and on the extent of serpentinization at depth.

Different approaches have been developed to address these issues, focusing either on the rock or on the fluid phase. Among them, oxygen isotope ratios of serpentinized peridotites have been widely used. They allow estimations of serpentinization temperatures (Früh-Green et al., 1996; Saccocia et al., 2009; Wenner and Taylor, 1971; Zheng, 1993) or time-integrated water-rock ratios (Taylor, 1977; Sakai et al., 1990), and allow the isotopic composition of the serpentinizing fluids to be calculated (Agrinier and Cannat, 1997). These results can be compared to constraints derived from other methods. For instance, experimental studies (e.g., Allen and Seyfried, 2003; Lafay et al., 2012; Malvoisin et al., 2012) allow correlation of mineralogical assemblages (e.g., serpentine versus talc after orthopyroxene, or presence of magnetite) to specific temperature ranges (Bach et al., 2004; Klein et al., 2014). Thorough description of textural sequences help to qualitatively estimate the evolution of water-rock ratios and the openness of the system with progressive exhumation and fluid-rock interaction (Andreani et al., 2007; Rouméjon and Cannat, 2014; Viti and Mellini, 1998). Finally, geochemical (Boschi et al., 2008; Delacour et al., 2008; Paulick et al., 2006) and petrological studies in general (Bach et al., 2004, 2006; Boschi et al., 2006; Rouméjon et al., 2015, 2018) provide additional

* Corresponding author.
E-mail address: stephane.roumejon@gmail.com (S. Rouméjon).

https://doi.org/10.1016/j.lithos.2018.09.021
0024-4937/

information on the conditions of serpentinization, such as the redox state or the mobility of chemical elements.

The composition of serpentinizing fluids cannot be measured at depth and is hypothesized to be similar to that of fluids escaping at hydrothermal vents. The nature of the fluids venting on the seafloor depends on the lithologies they interact with at depth. At Atlantis Massif (MAR, 30°N), the Lost City hydrothermal field is associated with low temperature (<100 °C), alkaline (pH 9–11), H_2– and CH_4-rich fluids, assumed to have interacted primarily with peridotites (Kelley et al., 2001, 2005; Kelley and Shank, 2010). In contrast, seawater-derived hydrothermal fluids interacting with gabbroic intrusions within peridotite lead to warmer (365 °C), acidic (pH ~3), sulfur-rich fluids such as at the Rainbow hydrothermal field (MAR, 36°N; Douville et al., 2002). The oxygen isotope composition of these fluids varies from a seawater-dominated composition ($\delta^{18}O \approx 0$–0.1‰) such as at Lost City (Atlantis Massif; Früh-Green et al., 2003) to hydrothermally altered seawater ($\delta^{18}O = 2.4$‰) influenced by the interaction with underlying lithologies, such as at the Snake Pit vent field (MAR, 23°N; Campbell et al., 1988).

Until recently, oxygen isotopes in serpentinized peridotites were only measured in bulk rocks or serpentine separates, targeting the whole sample or only specific textures (e.g., Agrinier and Cannat, 1997; Boschi et al., 2008; Früh-Green et al., 2004; McCaig et al., 2010; Rouméjon et al., 2015; Wenner and Taylor, 1971). The development of serpentine standards for ion microprobe analyses (Scicchitano et al., 2018) now allows studying the oxygen isotope behavior in serpentine minerals at scales previously unreachable (< 100 μm), and therefore provides new opportunities to evaluate isotopic heterogeneity in alteration textures.

This study focuses on the Atlantis Massif and the easternmost SWIR (62–65°E). In addition to detailed characterization of serpentine textures, we take advantage of in-situ oxygen isotope analyses in serpentine minerals to 1) follow the isotopic evolution of serpentine during exhumation, 2) study small scale heterogeneities of isotopic exchange and fluid-rock interaction, 3) derive constraints on the conditions of serpentinization (temperature, water-rock ratio, composition of the fluids), and 4) compare the two areas and investigate the influence of the gabbros on the serpentinization process.

2. Geological settings and sampling

2.1. Atlantis Massif (MAR, 30°N)

The Atlantis Massif is a 1.5–2-m.y.-old, dome-shaped bathymetric high (Blackman et al., 1998; Cann et al., 1997) located at 30°N along the slow-spreading MAR (Fig. 1a; 24 mm yr^{-1} full spreading rate; Zervas et al., 1995). It lies on the western flank of the axial valley and is bordered on the south by the Atlantis Fracture Zone. While a suite of mafic rocks, with a minimum thickness of 1400 m, forms the corrugated central dome (Blackman et al., 2006; Ildefonse et al., 2007), the non-corrugated southern wall of the massif is dominated by altered ultramafic rocks (~70%) that were intruded by gabbros before the onset of alteration (~30%; Blackman et al., 2002; Karson et al., 2006; Früh-Green et al., 2017). Samples recovered by dredges, dives and drilling on the south wall show that alteration of the peridotites is heterogeneous throughout the massif at scales of a few hundred meters to a kilometer. These heterogeneities are linked to the distribution of the fluid pathways during exhumation and to the presence of altered gabbroic intrusions (Rouméjon et al., 2018), in particular producing significant talc metasomatism in the deformed layers of the detachment fault zone (Boschi et al., 2006).

In this study, we used five serpentinized harzburgites and one dunite (Table 1) recovered by drilling during International Ocean Discovery Program (IODP) Expedition 357 (Oct.-Dec. 2015, RRS James Cook; Früh-Green et al., 2017). These samples are representative of the specific alteration that occurred in each hole, considered as independent

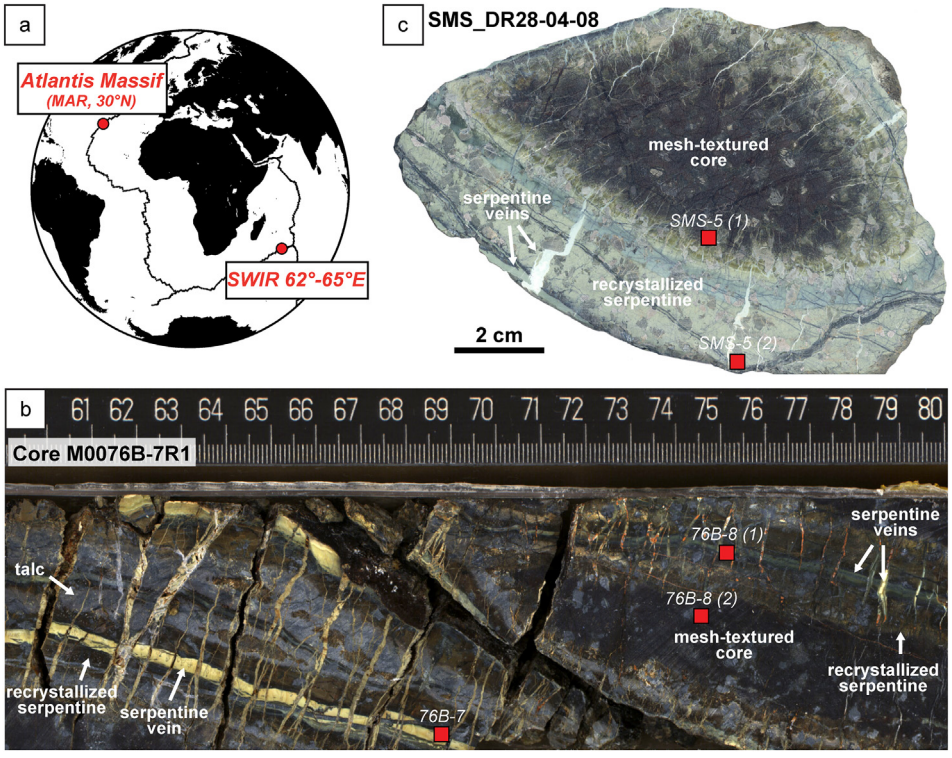

Fig. 1. a) Location of the studied serpentinized peridotites, drilled at Atlantis Massif along the Mid-Atlantic Ridge (MAR, 30°N) during IODP Expedition 357 (Früh-Green et al., 2017), and dredged along the Southwest Indian Ridge (SWIR) between 62°E and 65°E during the Smoothseafloor cruise (Sauter et al., 2013). b) Portion of Atlantis Massif Core M0076B-7R1 from which samples 76B-7 and 76B-8 were extracted, and c) Sample SMS_DR28-04-08 (SMS-5) dredged along the SWIR. These two serpentinized harzburgites exhibit the characteristic sequence of successive serpentinization textures targeted in this study: a mesh-textured core overprinted by rims of recrystallized serpentine and crosscut by serpentine veins (+ talc at Atlantis Massif).

Table 1
Lithological and textural description of the 11 serpentinized peridotites targeted for in-situ oxygen isotope analyses in this study.

Sample	Expedition	Site/Hole	Core/Section	Interval (cm)	Protolith	Relicts	Mesh texture	Bastite	Serpentine 2	Antigorite	Fibrous veins	Banded veins
68B-1	357	68B	4R1	14–17	harzburgite	ol, opx, cpx	**X**	o	o	o	o	
69A-6	357	69A	10R3	10–12	dunite		**X**				o	
71C-5	357	71C	9R1	24–26	harzburgite		**X**	**X**		**X**	**X**	
72B-1	357	72B	8R1	43–46	harzburgite	ol	**X**		o			o
76B-7	357	76B	7R1	68–71	harzburgite			o	**X**	**X**		**X**
76B-8	357	76B	7R1	74–77	harzburgite		**X**	**X**	**X**	o	o	**X**
Sample	Expedition	Dredge	Rock type	Sample number								
SMS-1	SMS	05	03	26	harzburgite		**X**	o	**X**	**X**	o	o
SMS-2	SMS	13	04	04	harzburgite			**X**	o	**X**		o
SMS-3	SMS	17	04	04	harzburgite	ol, opx, cpx	**X**	**X**			**X**	
SMS-4	SMS	17	04	66	dunite	ol, opx	**X**	o		**X**	o	
SMS-5	SMS	28	04	08	harzburgite		**X**	**X**	**X**		o	

ol: olivine, opx: orthopyroxene, cpx: clinopyroxene; o: texture present in the sample; **X**: texture successfully analyzed with SHRIMP.

portions of the footwall with their own unique history of fluid-rock interaction. The samples have been the subject of detailed textural, mineralogical and in-situ major and trace element chemical characterization (Rouméjon et al., 2018) that allowed the following conclusions to be derived: two samples, 68B-1 and 71C-5, record long-lasting and intense pervasive fluid-rock interaction during exhumation, while samples 69A-6 and 72B-1 underwent limited pervasive fluid-rock interaction. Samples 68B-1 and 72B-1 interacted with fluids that participated in the alteration of gabbros, while samples 69A-6 and 71C-5 were altered in a peridotite-dominated environment. Samples 76B-7 and 76B-8 originate from the same core (Fig. 1b) that shows a transition between moderate, pervasive fluid-rock interaction and subsequent, more intense and localized fluid-rock interaction associated with moderate amounts of altered gabbros. All these samples contain magnetite which, combined with reinterpreted bulk rock oxygen isotopes data (Boschi et al., 2008), point to serpentinization temperatures in the range of 200–350 °C.

2.2. Easternmost Southwest Indian Ridge (62–65°E)

The easternmost part of the SWIR, west of the Rodrigues triple junction, is an ultraslow spreading ridge (Fig. 1a; 14 mm yr^{-1} full rate; Patriat et al., 2008) and is recognized as a nearly amagmatic end-member in the global ridge system (Cannat et al., 1999; Dick et al., 2003). Magmatism is concentrated in localized volcanic domains, and the low magmatic supply results in a ~3.5 km-thick crust on average (Cannat et al., 2006; Minshull et al., 2006; Muller et al., 1999). The volcanic domains are laterally discontinuous and separated by ultramafic-dominated domains that can extend up to 50 km along-axis and be continuously produced during periods of up to 11 Myr (Sauter et al., 2013). In these domains, the seafloor, referred to as "smooth seafloor" (Cannat et al., 2006), is characterized by a smooth topography made up by broad and rounded bathymetric highs oriented parallel to the ridge axis. Both geophysical data (Cannat et al., 2006) and rock samplings (dredges and dives; Sauter et al., 2013; Cannat et al., 2017) indicate that wide portions of the seafloor are dominated by peridotites with minor gabbros (< 3%) and localized basaltic eruptions. Exhumation occurs along detachment faults that frequently switch polarity, cross-cutting earlier ones, leading to the smooth topography.

We selected four serpentinized harzburgites and one dunite (Table 1) dredged during the Smoothseafloor cruise (Oct. 2010, R/V Marion Dufresne; Sauter et al., 2013) between 62 and 65°E. The sampled smooth seafloor domains are both on- and off-axis and have a maximum age of ~5.9 Ma (magnetic anomaly C3An.y; Sauter et al., 2009). The samples benefit from previous detailed textural and mineralogical characterization, with a number of them also characterized for in-situ major and trace element geochemistry (Rouméjon et al., 2015; Rouméjon and Cannat, 2014). They were interpreted to record a multi-stage serpentinization process during exhumation, in an amagmatic context. Oxygen isotope analyses of these rocks were performed previously on local bulk separates extracted from the different serpentine textures. Together with the presence of magnetite, they record serpentinization temperatures in the range of 200–350 °C under increasing time-integrated fluid-rock ratios (Rouméjon et al., 2015).

3. Methods

3.1. Sample preparation

Textures and mineralogical assemblages were identified with optical microscopy and micro-Raman spectroscopy on 80-μm-thick thin sections. Seventeen pieces of maximum 3 by 3 mm were cut out of 11 thin sections using a diamond wire sawing machine. At the Australian National University (ANU), hundred-μm-sized fragments of reference materials were handpicked and mounted together in epoxy disks as closely as possible. After drying overnight, the mounts were polished and cut to extract a block containing the reference materials. Each reference material block contained 20 fragments of San Carlos olivine, 30 fragments of Cerro del Almirez antigorite (sample Al06-44A; Padrón-Navarta et al., 2011), 10–15 fragments of lizardite and two fragments of chrysotile (from the Mineralogical Collection at the Research School of Earth Sciences), one with horizontally-oriented fibers and one with vertically-oriented fibers (see Scicchitano et al. (2018) for more details on reference materials). A reference material block was mounted with three to four pieces of sample and the whole polished to ensure a flat target surface.

Backscattered electron maps of each of the five mounts were produced using a JEOL JSM6610A Scanning Electron Microscope (SEM). Maps were constructed from a mosaic of images obtained using a 1-mm step between pictures under a 120-times magnification and a 15 kV-voltage. Reflected light photos were also taken to image surface irregularities and help orient the samples during analyses. After removal of the carbon coating, the mounts were cleaned using an ethanol bath, a detergent bath with ultrasound, and then dried in a vacuum oven (60 °C) for a few days.

3.2. Electron microprobe analyses

Major elements were acquired on a JEOL JXA-8200 electron microprobe at the ETH Zürich, as close as possible to the SHRIMP targets. We used a 15-kV acceleration voltage, a 10 nA beam current, and a 5-μm spot size. Each element was standardized using natural and synthetic mineral standards and measured for 30 s (10 s for the background, 20 s for the peak). The data were averaged by texture and given in Table A1**,** which includes a compilation of datasets previously acquired on samples from SWIR (Rouméjon et al., 2015) and Atlantis Massif (Rouméjon et al., 2018).

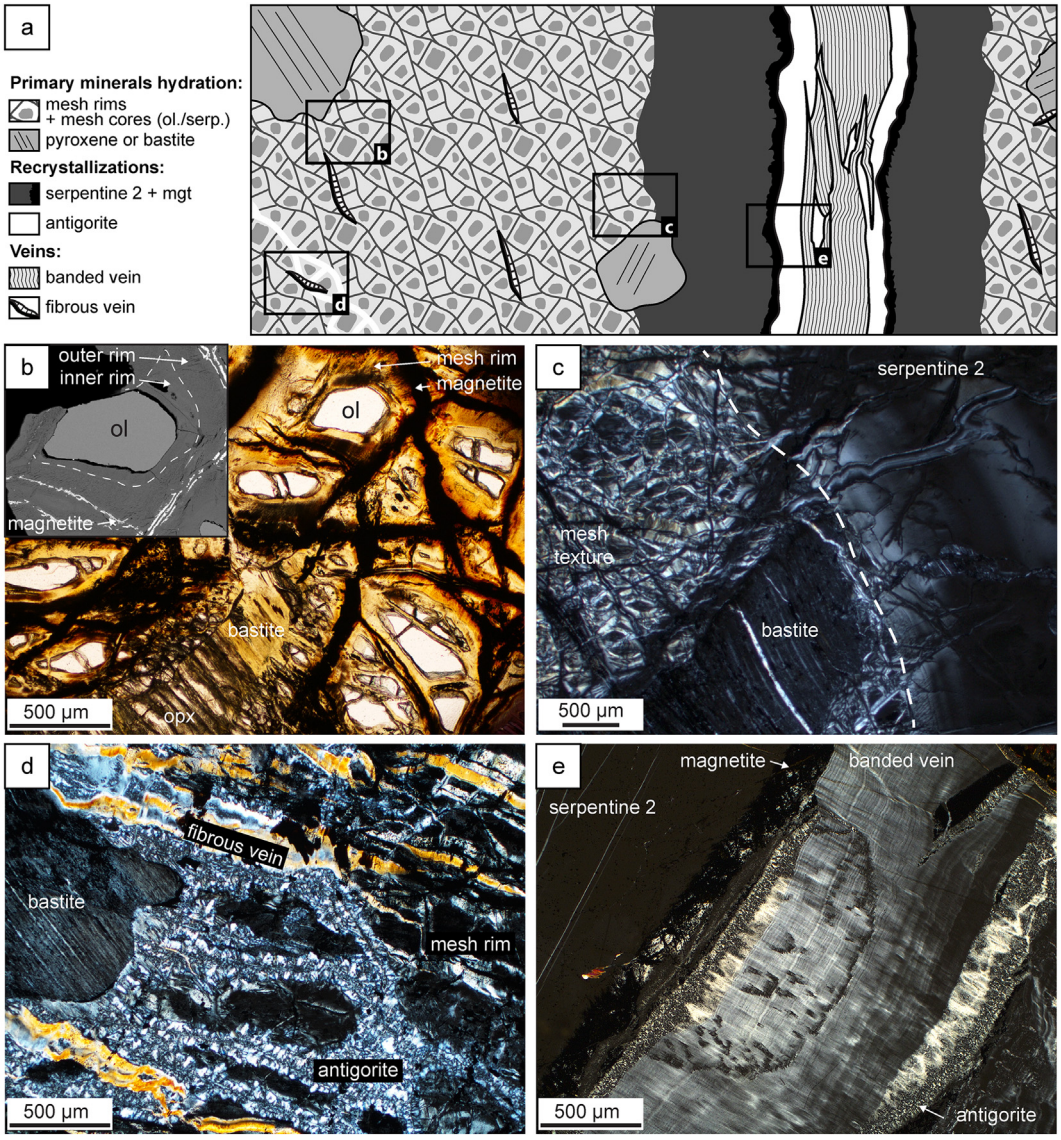

Fig. 2. a) Compilation sketch summarizing the sequence of serpentine textures targeted in this study at both the Atlantis Massif and SWIR. b) Partially serpentinized olivine and orthopyroxene leading to the mesh and bastite textures, respectively (sample SMS-4). Inset in Fig. 3b) shows Scanning Election Microscopy (SEM) image of a mesh cell delimited by magnetite concentrations along interconnected microfractures. The mesh cell is composed of a serpentine mesh rim (outer + inner) and a mesh core containing an olivine relict. c) Transition between a fully serpentinized mesh texture and the chrysotile-dominated serpentine 2 recrystallization texture (sample SMS-5). d) Fully serpentinized mesh texture and bastite (sample 71C-5). The mesh rims are overprinted by antigorite recrystallization and all are crosscut by chrysotile fibrous veins. e) Serpentine 2 domain replaced by antigorite and crosscut by a banded vein (sample 76B-8). Magnetite is concentrated at the serpentine 2-antigorite transition. All photomicrographs taken under cross-polarized light. See Table 2 for a summary of the lithological and textural characteristics of the individual samples.

3.3. Sensitive high-resolution ion microprobe (SHRIMP) analyses

The mounts were first coated with a 42-Å-thick layer of gold. SHRIMP analyses were conducted with a 12 nA Cs^+ primary beam focused to a spot size of ~30 µm. An electron gun provided charge neutralization of the insulator mineral surfaces. Each analysis consisted of a pre-burn phase of 2 min, followed by five or six 20 s scans. The Cerro del Almirez antigorite was used as the primary serpentine reference material ($\delta^{18}O = 8.30 \pm 0.12$‰; Scicchitano et al., 2018) while San Carlos olivine (SCO, $\delta^{18}O = 5.27$‰; Ahn et al., 2012), lizardite, and chrysotile secondary reference material allowed monitoring mineralogical matrix bias ($\delta^{18}O = 5.26$, and 4.37‰; Scicchitano et al., 2018). The antigorite standard was analyzed twice every eight sample spots, and the SCO twice every 16 sample spots. Four analyses of each of the lizardite and the two orientations of chrysotile were added to each mount. The repeatability of the antigorite primary reference material was between 2.9 and 4.1‰ and the uncertainty on the mean value was 0.60‰ (2 σ-error). Measured average $\delta^{18}O$ for the secondary reference materials SCO, lizardite and chrysotile were 5.29 ± 0.20, 5.20 ± 0.25, 4.51 ± 0.28‰, respectively, so that the measured average biases relative to antigorite were 0.02, −0.06, and 0.14‰. These measured biases were subtracted from sample analyses for lizardite and chrysotile. Internal uncertainties on individual measurements were typically on the order of 0.10–0.15‰ (2 σ-error). Overall, the external uncertainty of sample $\delta^{18}O$ measurements (propagated uncertainty including the uncertainty on the reference material mean value, uncertainty on the measured matrix bias and internal analytical uncertainty) was on the order of 0.7–0.9‰.

Using the SHRIMP data reduction program POXI, we applied background and electron-induced secondary ion emission (EISIE; Ickert et al., 2008) corrections, and instrumental mass fractionation drift corrections, using a linear regression through the reference material measurements, where necessary. Measured sample oxygen isotope ratios are

reported as bias-corrected values in $\delta^{18}O$ versus VSMOW (Vienna Standard Mean Ocean Water, in ‰).

In the initial dataset, several $\delta^{18}O$ values were unexpectedly low for serpentine (down to −16‰). Most of these suspect values corresponded to textures with a potential significant porosity based on optical microscopy and SEM images (Fig. 2a and b). We tested this hypothesis by analyzing all the SHRIMP targets with the electron microprobe. Except for primary minerals, all the targets had a structural formula of a serpentine and hence did not include significant traces of other mineral components (Fig. A1). However, most of the textures associated with low $\delta^{18}O$ had a total oxide content (in weight per cent, wt %) below 80 wt%, i.e. below typical serpentine values (~85 wt%). These total oxide contents linearly decreased with the measured $\delta^{18}O$ (Fig. 2c). We therefore discarded these $\delta^{18}O$ values. We also discarded $\delta^{18}O$ values obtained in two fresh orthopyroxenes as the absence of a proper pyroxene standard led to values (3.7–4.9‰) out of the classic range for orthopyroxenes (5.4–6.1‰; Mattey et al., 1994) and no textural and major element evidence pointed towards a secondary origin of the orthopyroxenes.

4. The sequence of serpentinization textures

Sampling at the Atlantis Massif and SWIR recovered highly to fully serpentinized peridotites. The primary minerals are replaced by successive generations of serpentine textures (Rouméjon et al., 2015, 2018) indicating that serpentinization is a multistage process, as previously reported in various contexts (e.g., Andreani et al., 2007; Kahl et al., 2015; Viti and Mellini, 1998). Despite minor differences between the two locations and even between holes at Atlantis Massif, the sequence of serpentine textures is very similar. In hand specimen (Fig. 1b and c), the sequence consists of ~10-cm-long mesh-textured relict domains overprinted at their edges by recrystallized serpentine and veins, with later talc at Atlantis Massif. The textures indicate the transition between an early pervasive hydration and a later localization of fluid flow under more open conditions. The 11 selected samples from the two areas contain either the full sequence or only part of it (Table 1).

The textural sequence targeted for oxygen isotopes measurements at both the Atlantis Massif and SWIR is schematically shown at the thin section scale in Fig. 3a. Four of the analyzed samples still contain olivine relicts and three of them have orthopyroxene and clinopyroxene relicts. Olivine serpentinization leads to a ubiquitous mesh texture (e.g., Rouméjon and Cannat, 2014; Viti and Mellini, 1998; Wicks and Whittaker, 1977). An interconnected, tightly-spaced (≤100 μm), pervasive network of microfractures crosscuts the olivine, defining mesh cells (Fig. 3b). The microfractures serve as pathways allowing fluids to react with the olivine and to first produce lizardite mesh rims. As a second step, the olivine that remains in the mesh core is replaced by disoriented and finely-grained lizardite and/or chrysotile which gives an isotropic aspect to the mesh cores under cross-polarized light. Part of the iron mobilized during the conversion of olivine to serpentine is incorporated as magnetite in the mesh rims and concentrates along the microfracture planes. No brucite was observed in any of our samples. In the At SWIR samples, some mesh rims consist of two concentric parts (inset in Fig. 3b): the outer rim is in contact with the microfracture and magnetite, and the inner rim is in contact with the mesh core. The outer rims result from interaction between the fluids and the initial mesh rims that locally leads to the replacement of lizardite by chrysotile (e.g., sample SMS-1) and to magnetite concentrations. The inner rims correspond to remnants of the initial mesh rims so that the chronology of emplacement is: inner mesh rims, mesh cores, outer mesh rims. Orthopyroxenes

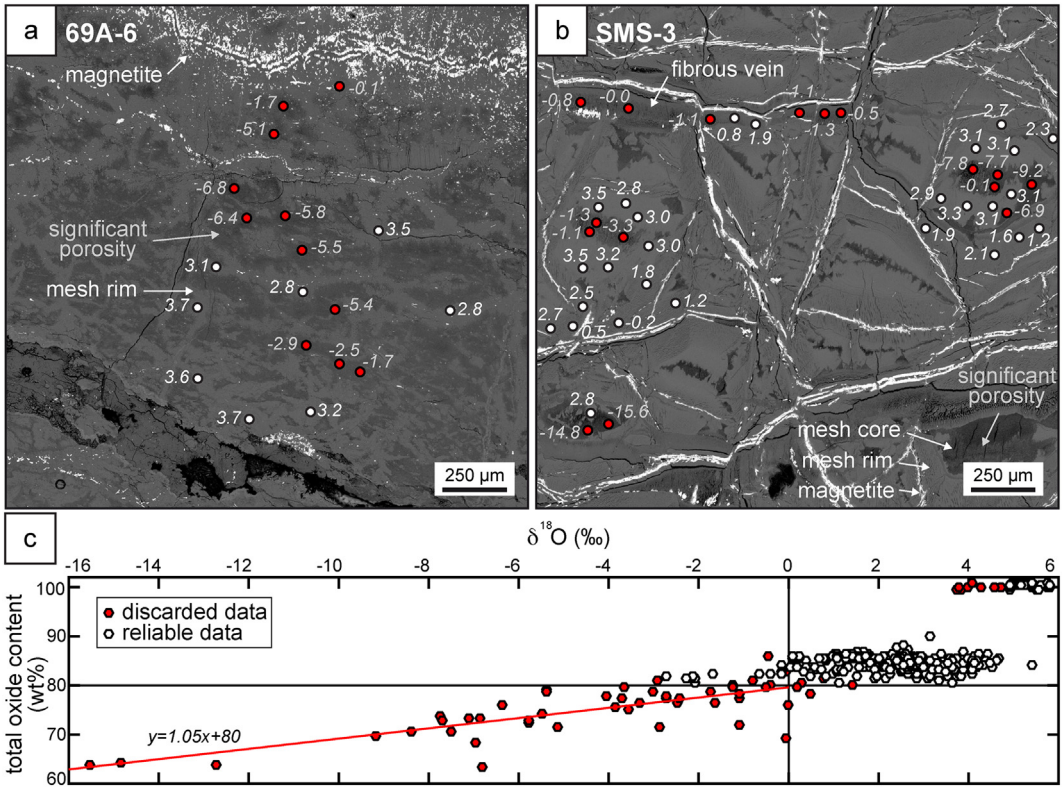

Fig. 3. Criteria for selection of the reliable $\delta^{18}O$ data. a) SEM map of the mesh texture in sample 69A-6. The negative $\delta^{18}O$ values are in the dark grey areas that are suspected to be porous. The lighter grey network corresponds to mesh rims with $\delta^{18}O$ values more common for serpentine. b) In sample SMS-3, the negative $\delta^{18}O$ are associated with the dark grey mesh cores or with portions of the fibrous vein. c) $\delta^{18}O$ versus total oxide content in all the minerals and textures targeted. The negative $\delta^{18}O$ values correlate with total oxide contents below 80 wt% (i.e., below the typical value of ~85 wt% for serpentine) confirming a significant porosity in serpentine. The $\delta^{18}O$ values measured in pyroxenes (red dots around 100 wt%) were discarded due to the lack of an appropriate matrix-matched pyroxene standard.

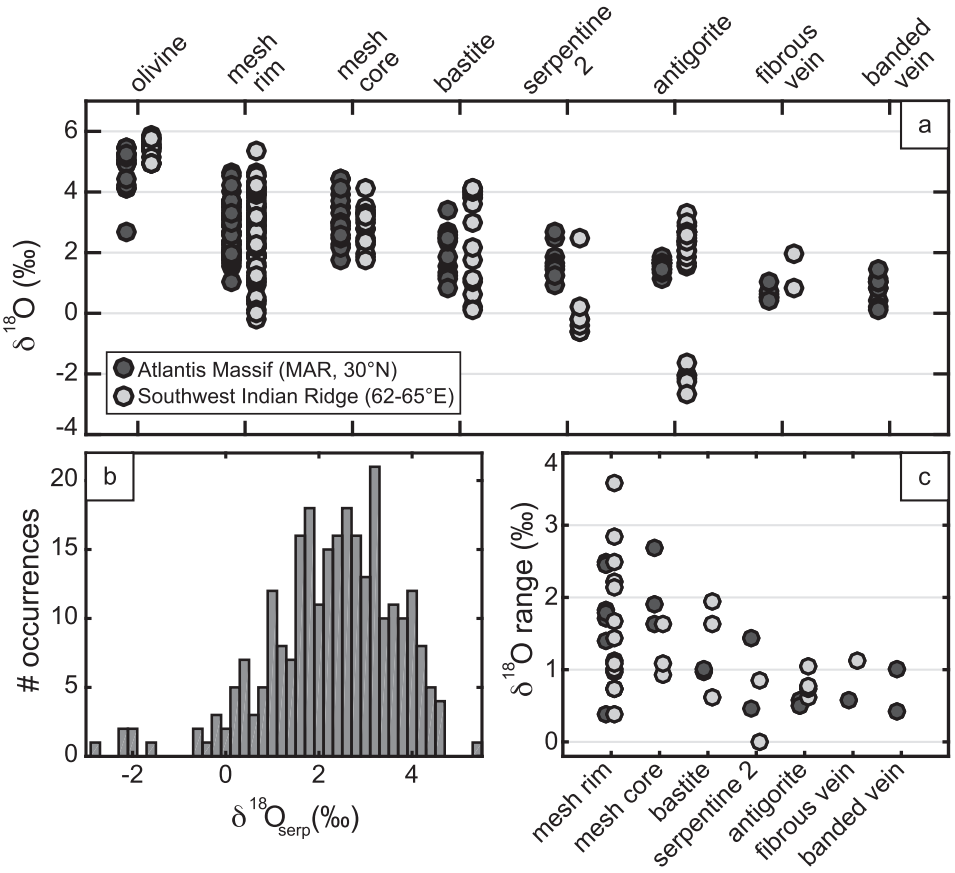

Fig. 4. a) Reliable oxygen isotope ratios ($\delta^{18}O$) measured in the olivine and serpentine textures in the Atlantis Massif and SWIR samples. Serpentine minerals have lower $\delta^{18}O$ values than the olivine and show an overall decrease in $\delta^{18}O$ with the sequence. b) Histogram of the reliable $\delta^{18}O$ in serpentine minerals. c) $\delta^{18}O$ range ($\delta^{18}O_{max} - \delta^{18}O_{min}$) for each serpentine texture. The range is maximal in the mesh texture and bastite and decreases in the subsequent textures suggesting homogenization of the isotopic composition with increasing fluid-rock interaction.

are altered to bastite pseudomorphs in nine samples or to talc, tremolite and/or chlorite in several samples. Clinopyroxenes are either fresh or altered to talc or tremolite.

In seven samples, the mesh texture is locally replaced by a homogeneous texture, dominated by chrysotile and is isotropic under cross-polarized light (Fig. 3c). The sharp transition between the mesh texture and this texture, referred to as serpentine 2, implies replacement of lizardite by chrysotile via dissolution-recrystallization processes (Rouméjon et al., 2015). It occurs as bands, crosscutting the sample, that develop along continuous microfractures of the mesh texture and laterally grow up to a few centimeters in width. Serpentine 2 is interpreted as a marker of preferential fluid pathways that led to intense fluid-rock interaction in specific domains of the peridotite. Lizardite replacement by chrysotile is driven by the increasing degree of supersaturation of the fluids with respect to serpentine and by the geometry of the nucleation site (Grauby et al., 1998; Normand et al., 2002). Magnetite is rare in serpentine 2, and rather concentrates at the contacts with the antigorite/banded vein domains developed in the center of the bands (Fig. 3e).

Antigorite forms interlocking to interpenetrating textures and shows two types of occurrence: 1) in the variably serpentinized mesh texture, as thin planes continuous across the thin section (Fig. 3d) and develops along interconnected microfractures at the expense of lizardite mesh rims; 2) at the center of serpentine 2 domains, replacing chrysotile. The later banded veins break apart the antigorite texture into elongated domains (Fig. 3e). In both cases, antigorite crystallization is assumed to be triggered by interaction with fluids slightly enriched in Si (e.g., Rouméjon et al., 2015, 2018; Schwartz et al., 2013).

The banded veins are made up of ~1-μm-thick bands of serpentine (chrysotile ± polygonal serpentine ± lizardite), oriented parallel to the vein wall, that correspond to successive opening increments (crack-seal mechanism; Andreani et al., 2004; Fig. 3e). They develop as en echelon lens-shaped veins, up to several millimeters in width, that eventually join to produce the continuity observed in hand specimens (Fig. 1b and c). Fibrous veins are extensive lens-shaped veins, with chrysotile fibers parallel to the opening direction and joining the vein walls. They develop parallel to the mesh texture microfractures or during later stages in the serpentinization history, for instance orthogonally crosscutting banded veins. Some samples also contain later serpentine veins, with various shapes and textures, but as no systematic relationships were found at either location we have not incorporated these into this study.

5. Results

5.1. Oxygen isotope data

Five of the six olivine grains analyzed by SHRIMP and standardized to SCO have average $\delta^{18}O$ values between 5.1 and 5.6‰, with a maximum intracrystalline variability of 0.9‰ (Fig. 4a,Table 2). The sixth sample (72B-1) has an average value of 3.9‰ including one analysis strongly departing from the rest (2.7‰). All the serpentine minerals have lower $\delta^{18}O$ values than the precursor olivine, with $\delta^{18}O$ ranging between −2.7 and 5.4‰, although most values lie between 1 and 4‰ (Fig. 4b). Only two textures have negative values that are not associated with a low total oxide content: antigorite in sample SMS-2 and

Table 2
All reliable $\delta^{18}O$ data, with the average value, standard deviation, and range ($\delta^{18}O_{max}$ - $\delta^{18}O_{min}$) within each texture.

Sample	Texture	$\delta^{18}O$ (‰)									Average	Std	Range
68B-1	olivine	4.98	4.99	5.03	5.07	5.28					5.07	0.12	0.30
	mesh rim	2.21	2.73	2.93	3.15	4.05	4.68				3.29	0.91	2.46
	olivine	5.18	5.25	5.25	5.43	5.47					5.31	0.12	0.28
	mesh rim	1.54	2.04	2.31	2.67	2.90	3.37				2.47	0.65	1.83
	mesh rim	1.07	1.99	2.11	2.22	2.40	3.52				2.22	0.79	2.45
	mesh core	1.80	2.16	2.28	3.46	3.51	4.47				2.95	1.03	2.67
69A-6	mesh rim	2.84	2.84	3.14	3.21	3.54	3.64	3.71	3.74	4.54	3.47	0.53	1.70
71C-5	mesh rim	1.69	1.75	1.76	1.84	1.87	2.07				1.83	0.14	0.39
	bastite	0.85	1.13	1.25	1.31	1.54	1.81				1.31	0.33	0.96
	antigorite	1.19	1.43	1.65	1.68	1.72	1.77				1.57	0.22	0.58
	fibrous v.	0.47	0.49	0.57	0.59	0.73	1.03				0.65	0.21	0.56
72B-1	olivine	2.65	4.13	4.14	4.26	4.40					3.92	0.72	1.75
	mesh rim	2.41	3.12	3.27	3.57	3.73	4.21				3.39	0.61	1.80
	mesh core	2.49	3.29	3.73	3.90	4.13	4.40				3.65	0.68	1.91
76B-7	serp. 2	1.25	1.59	1.66	1.83	2.52	2.66				1.92	0.55	1.41
	antigorite	1.35	1.41	1.51	1.64	1.67	1.84				1.57	0.18	0.49
	banded v.	0.11	0.24	0.40	0.80	0.85	1.10				0.58	0.39	1.00
76B-8	mesh rim	1.87	1.96	2.55	2.63	2.95	3.25				2.53	0.54	1.37
	mesh core	2.61	2.75	2.93	3.01	3.02					2.86	0.18	0.41
	bastite	2.38	2.44	2.45	2.55	2.65	3.39				2.64	0.38	1.00
	serp. 2	0.98	1.25	1.41							1.21	0.22	0.43
	banded v.	1.01	1.04	1.06	1.41						1.13	0.19	0.40
SMS-1	inner rims	3.10	3.23	3.34	3.52	3.65	3.81				3.44	0.27	0.71
	mesh core	1.89	2.25	2.37	2.51	2.79	2.81				2.44	0.35	0.92
	outer rims	0.97	1.05	1.12	1.54	1.93	1.97				1.43	0.45	1.01
	serp. 2	2.52									2.52		
	antigorite	2.10	2.33	2.39	2.49	2.64	2.69				2.44	0.22	0.59
	antigorite	1.59	1.69	1.91	2.05	2.23	2.35				1.97	0.30	0.75
SMS-2	bastite	0.09	0.22	0.67	1.06	1.09	1.71				0.81	0.61	1.62
	antigorite	−2.70	−2.26	−2.15	−2.07	−2.06	−1.68				−2.15	0.33	1.02
SMS-3	olivine	5.42	5.47	5.52	5.62	5.74					5.55	0.13	0.32
	inner rims	2.83	2.84	2.89	3.49	3.91	3.95	4.51			3.49	0.66	1.68
	outer rims	1.33	1.66	1.88	2.29	2.40					1.91	0.44	1.07
	olivine	4.93	5.39	5.55	5.82						5.42	0.37	0.89
	inner rims	3.05	4.10	4.17							3.77	0.63	1.13
	outer rims	0.31	0.37	0.44	1.06	1.82	1.82	2.15	2.45		1.30	0.86	2.13
	bastite	2.12	3.04	3.77	3.81	3.87	4.05				3.45	0.73	1.92
	inner rims	2.78	2.84	3.00	3.02	3.21	3.45	3.52			3.12	0.29	0.74
	outer rims	−0.16	0.48	1.19	1.82	2.45	2.69				1.41	1.12	2.85
	inner rims	2.91	3.13	3.14	3.14	3.16	3.26				3.12	0.11	0.34
	outer rims	1.24	1.57	1.91	2.12	2.27	2.65				1.96	0.50	1.41
	fibrous v.	0.81	1.94								1.38	0.80	1.13
SMS-4	olivine	4.91	4.96	5.17	5.41	5.73	5.79				5.33	0.38	0.87
	mesh rim	2.17	2.55	2.67	3.68	4.11	4.64				3.30	0.98	2.47
	mesh rim	0.04	0.15	2.27	2.67	2.70	3.64				1.91	1.48	3.60
	antigorite	2.55	2.71	2.72	2.88	3.01	3.28				2.86	0.26	0.74
SMS-5	mesh rim	3.19	3.87	4.06	4.07	4.09	4.15				3.90	0.36	0.96
	mesh core	1.79	1.99	2.39	3.12	3.28	3.42				2.67	0.70	1.63
	mesh rim	3.16	4.24	4.34	4.37	4.49	5.39				4.33	0.71	2.23
	mesh core	3.03	3.17	3.32	3.34	3.49	4.10				3.41	0.37	1.06
	bastite	3.56	3.96	4.06	4.07	4.15	4.16				4.00	0.22	0.60
	serp. 2	−0.63	−0.57	−0.41	−0.17	−0.16	0.20				−0.29	0.31	0.83

serpentine 2 in sample SMS-5. The overall $\delta^{18}O$ of the serpentine minerals decreases with the textural sequence, which is also verified sample by sample. Mesh rims and mesh cores share similar ranges and are comparable to bastites in a given sample. Values in subsequent recrystallization textures and veins differ at the two locations. At Atlantis Massif, the decrease in $\delta^{18}O$ is continuous. At SWIR, it is less pronounced for a given sample and the $\delta^{18}O$ of serpentine 2, antigorite or fibrous vein are either higher or lower than at Atlantis Massif. Finally, the variation in $\delta^{18}O$ within a given texture (Fig. 4c) is the highest in the mesh texture and bastites (up to 3.6‰) and is limited to <1.5‰ in the subsequent textures, indicating homogenization with increasing fluid-rock interaction.

Detailed analyses of the mesh texture reveal heterogeneous $\delta^{18}O$ values at the 100 μm scale. In partially serpentinized domains, narrow and magnetite-free mesh rims have the highest $\delta^{18}O$ (up to 4.6–4.7‰; Fig. 5a and b) while broad mesh rims with significant magnetite concentrations have the lowest (down to 2.2%). In the fully serpentinized mesh texture, the mesh rims contain magnetite and also show $\delta^{18}O$ values around 2.0–2.5‰ (e.g., sample 68B-1, Table 2). This suggests that $\delta^{18}O$ of the mesh rims decreases with on-going serpentinization after its initial formation. In Fig. 6a, we compare the $\delta^{18}O$ value of the domains making up the mesh texture in the Atlantis Massif samples. Considering only the mesh rims of fully serpentinized mesh textures, the Atlantis Massif samples can be divided into three groups: 1) samples 69A-6 and 72B-1, with most of the $\delta^{18}O$ values above 2.5‰; 2) samples 68B-1 and 71C-5, with most of the $\delta^{18}O$ values below 2.5‰; and 3) sample 76B-8, with intermediate values. The mesh cores share similar values. In contrast, in the SWIR samples, each domain with the mesh texture has homogeneous $\delta^{18}O$ values but the overall $\delta^{18}O$ decreases with the inner mesh rim (mostly >2.5‰), mesh core (intermediate), and outer mesh rim succession (mostly <2.5‰; Fig. 6b). At both locations, the lateral variability within a mesh rim (i.e. < 100 μm) can reach 0.5‰ for partially serpentinized mesh textures. This variability increases with higher degrees of serpentinization: up to 1‰ in inner and outer mesh rims (Fig. 5c and d) and up to 0.8‰ in mesh cores (e.g., sample SMS-5; Table 2).

The five analyzed bastites follow the average value of the mesh texture analyzed in the same sample and their $\delta^{18}O$ decrease with the

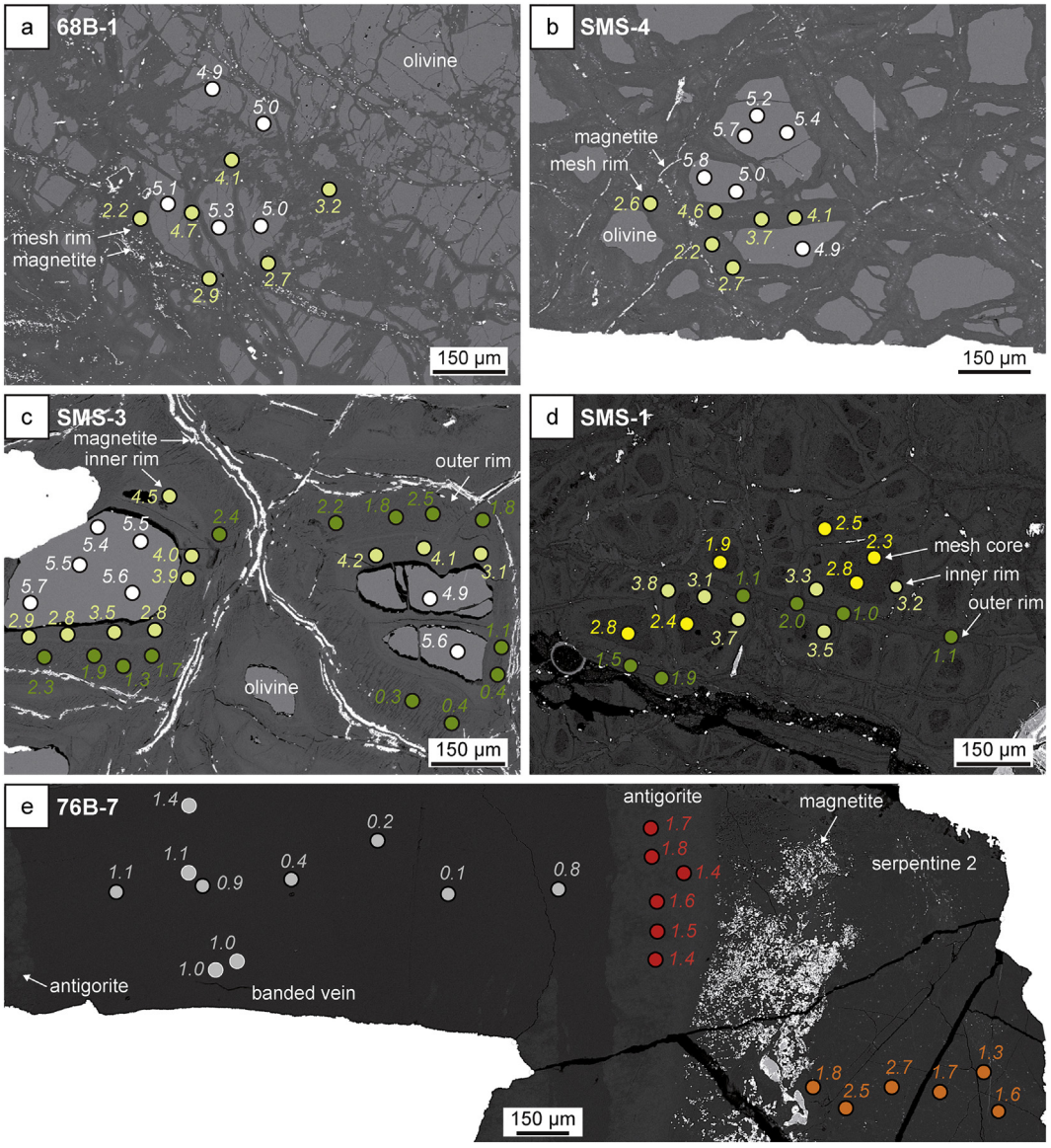

Fig. 5. Examples of $\delta^{18}O$ spatial variation across various textures and samples, reported on SEM images. In e), the grey dots with white contours are data measured in the banded vein of sample 76B-8 and reported here with respect of the distance from the vein wall.

serpentinization sequence. The partially serpentinized orthopyroxene of sample SMS-3 is associated with a partially serpentinized mesh texture and has a relatively high $\delta^{18}O$ (3.5‰; Table 2) compared to those associated with fully serpentinized mesh textures (sample 76B-8) ± antigorite (sample 71C-5) or serpentine 2 domains (sample SMS-2). Sample SMS-5 is the exception, with an average $\delta^{18}O$ of 4.0‰ in a fully serpentinized mesh texture. In addition, bastites contain a lateral variability reaching 2‰ within a few hundreds of microns. These variations are not linked to any visible textural or mineralogical feature (e.g., fractures or cleavage, core to rim transect) or any specific major element composition.

Serpentine 2 or antigorite recrystallizations and fibrous veins share limited intra-textural variability (<1.4‰). They exhibit no clear spatial gradients and generally have a lower $\delta^{18}O$ than the textures they postdate (e.g., Fig. 5e). In contrast, banded veins show lateral gradients across the vein. In Fig. 5e (sample 76B-7), $\delta^{18}O$ decreases from left to right across the vein (1.1 to 0.1‰) with the exception of a higher value (0.8‰) along the right wall of the vein. The decrease correlates with the left to right vein opening direction estimated from the discordant contact between the bands and the vein wall at vein tips (see Andreani et al., 2004). This suggests crystallization of serpentine with lower $\delta^{18}O$ with time. In addition, the ~500 μm-long, band-parallel profile realized in sample 76B-8 indicates that these veins are homogeneous in this direction (variability ≤0.4‰). Fig. 5e shows variations with distance from the wall and indicates that the $\delta^{18}O$ values match with those of sample 76B-7. This, together with the fact that these two samples are separated by a few centimeters in the same core drilled at the Atlantis Massif (Fig. 1b) and that $\delta^{18}O$ in the serpentine 2 domains are similar, allow us to conclude that the banded veins are homogeneous at least at scales of 10 cm but that the composition of the newly formed bands evolves with time. This homogeneity between the two samples also leads us to consider their textural sequences as one feature in the following discussion.

5.2. Major elements in serpentine minerals

The serpentine textures show negligible variability for most major elements. Only Si and Al show significant trends between the two

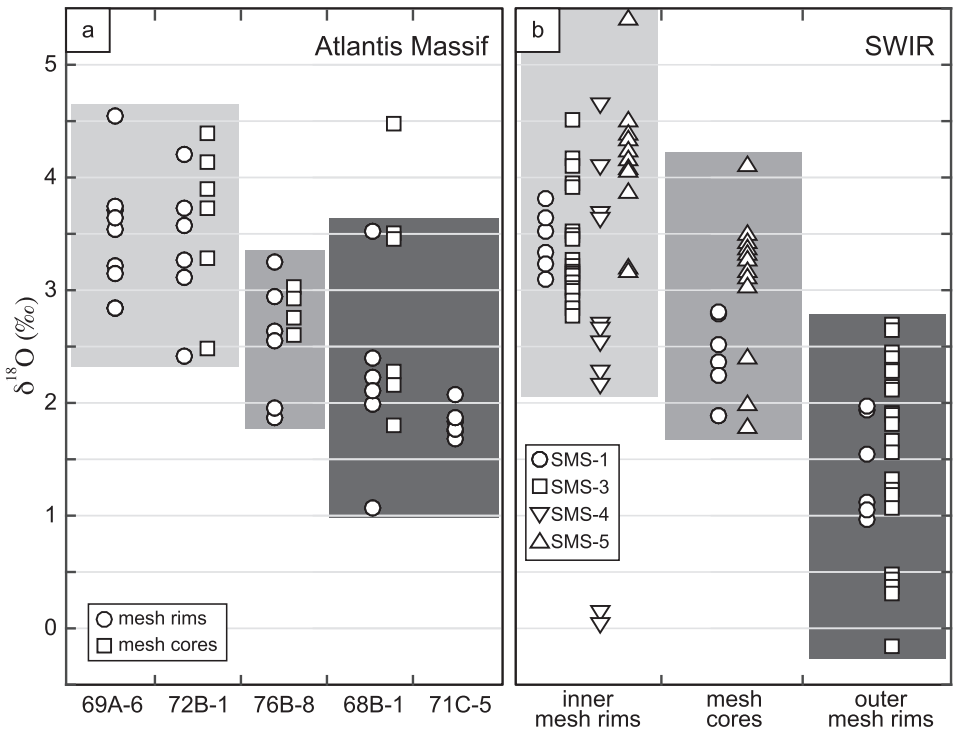

Fig. 6. $\delta^{18}O$ in the different domains making up the mesh texture in a) the Atlantis Massif samples and b) the SWIR samples (see text).

locations and between holes at the Atlantis Massif. The serpentine textures from the SWIR samples (grey fields in Fig. 7) are the most Al-rich, as reflected by their position along the Tschermak's substitution trend (Al replacing an octahedral or tetrahedral cation, Fig. 7a and b) and their departure from the brucite-serpentine-talc trend in the Si versus Mg + Fe space (Fig. 7c and d). The domains making up the mesh texture of the SWIR samples plot around stoichiometric serpentine with a slight depletion in Si for some of them (Fig. 7a and c), while the subsequent textures show Al and Si enrichments (Fig. 7b and d). The serpentine from the Atlantis Massif Site M0071 follows this behavior. Those from Holes M0069A, M0072B and M0076B plot along the brucite-serpentine-talc trend, around the stoichiometric serpentine but with variable amplitudes (Fig. 7c). They are all enriched in Si (in the serpentine-talc space in Fig. 7d) for the recrystallizations and veins. Serpentine textures from Hole M0068B are systematically Si-rich and always higher than the serpentine end-member. Note that such departures from stoichiometric serpentine towards brucite, talc, or chlorite are very limited and do not necessarily indicate that these phases are present, even as significant intergrowths, given the present scale of observation.

6. Discussion

6.1. Porosity in serpentine textures

In a previous study, serpentine separates were extracted from the same SWIR samples as those analyzed here (Rouméjon et al., 2015). Each separate targeted ~1cm^3 of the mesh texture, recrystallized serpentine, veins, or a combination of them (Table 3). Here we compare the $\delta^{18}O$ of these separates and the reconstructed $\delta^{18}O$ values calculated using the contribution of the textures analyzed in-situ. The relative contributions are determined by quantifying the area occupied by each texture in portions of SEM maps such as those presented in Fig. 5. In all cases, the reconstructed $\delta^{18}O$ values are lower than the serpentine separate $\delta^{18}O$ values. The differences are the highest for partially serpentinized mesh textures (2.6 and 3.4‰) and the lowest for the fully serpentinized mesh textures (0.9 and 1.1‰). They are intermediate for the serpentine 2 (2.2‰). Phases other than serpentine could contribute to these differences. The bulk separates consisted only of a serpentine powder after extraction of magnetite using a magnet and primary phases (olivine, pyroxenes) by settling in water. Considering that differences are higher for partially compared to fully serpentinized mesh textures, it is possible that removal of olivine and pyroxene relicts was not perfect, shifting the separates to higher $\delta^{18}O$ values. This however requires unrealistic modal amounts of primary minerals relicts in the preparation (e.g., 86% in mode for sample SMS-4) to explain the entire discrepancy so that this potential contribution is limited to negligible. The role of additional undetermined heavy phases in the mineral separates is unlikely as such phases are absent in thin sections (Rouméjon et al., 2015). Similarly, though magnetite concentrations were avoided, some grains may have been included in the in-situ measurements. We nevertheless estimate that their amount is too low to significantly shift the $\delta^{18}O$ to lower values. Part of these differences could also derive from the fact that the narrowest mesh rims, bearing the highest $\delta^{18}O$ values (e.g., Fig. 5), could hardly be analyzed due to the analysis spot size. The value used for the mesh rims and the resulting reconstructed values could therefore be underestimated, but such contribution is difficult to quantify. Finally, the systematic lower values of in-situ $\delta^{18}O$ could result from an analytical bias. Contrary to bulk rock or serpentine separate analyses that destroy the inter- and intracrystalline structures, in-situ analyses integrate the natural porosity of the serpentine textures. Such a porosity creates topography which can influence microprobe measurements (e.g., Kita et al., 2009), or could be filled by glue or epoxy during sample preparation, lowering the measured $\delta^{18}O$.

Serpentinized peridotites are recognized to host a significant porosity (e.g., Falcon-Suarez et al., 2017; Miller and Christensen, 1997). This comes from open fractures crosscutting the rock and whose network evolves with serpentinization due to the reaction-driven volume increase (e.g., Jamtveit et al., 2009; Plümper et al., 2012; Rouméjon and Cannat, 2014). This adds to the porosity of serpentine textures that

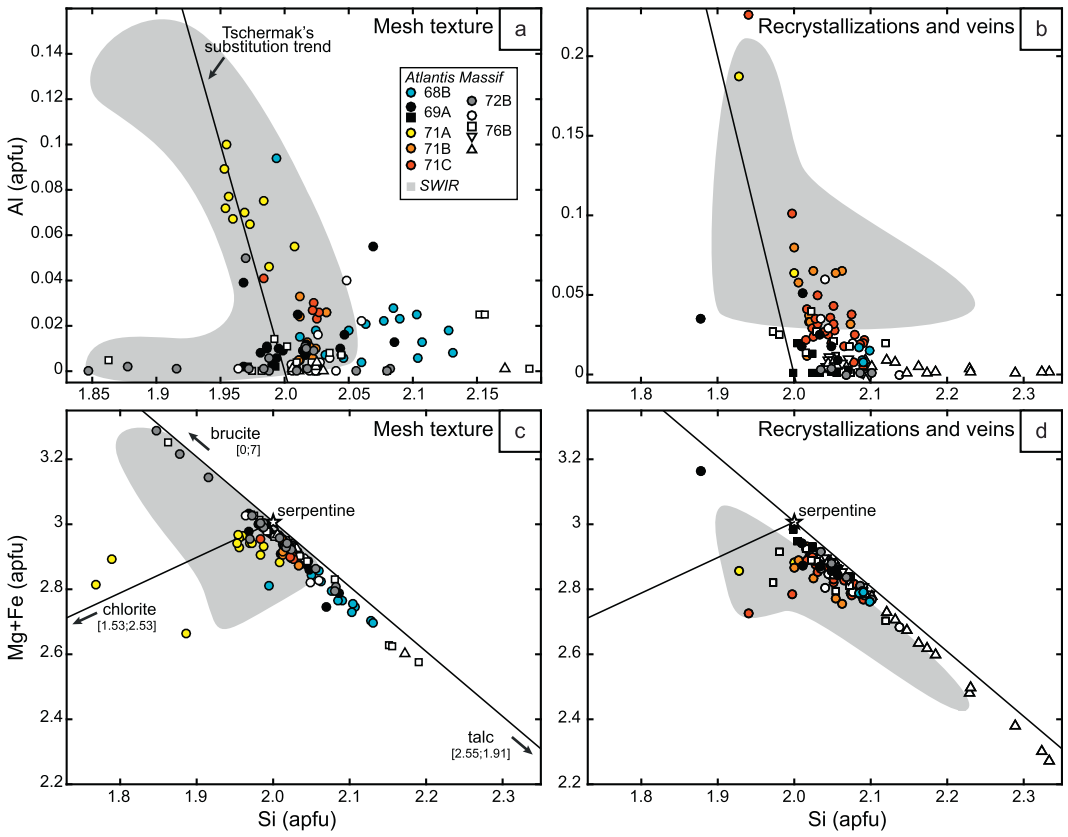

Fig. 7. Major element compositions of serpentine minerals in the Atlantis Massif (colored symbols) and SWIR (grey shaded fields) samples. Compositions are expressed in atoms per formula unit (apfu) on the basis of 7 oxygen atoms in the serpentine formula. Si, Mg, and Fe are substituted by Al in variable amounts (Tschermak's substitution trend in a) and b)) and departure from the brucite-serpentine-talc trend in c) and d). Si is variably enriched compared to Mg + Fe.

ranges from the micrometer scale as a result of phase dissolution (e.g., brucite or relict olivine) with increasing fluid flow (Jöns et al., 2017) down to the nanometer scale and the intracrystalline porosity associated with defects in serpentine (Tutolo et al., 2016). The serpentinization texture development indicates that at least part of this porosity is interconnected and forms a permeability network able to channel the hydrothermal fluids in abyssal peridotites. Veins represent the crystallization from a fluid in voids open along fractures and are therefore the most evident marker of permeability pathways through these rocks. The emplacement of multiple generations of veins can record the evolution of the openness of the system with exhumation of the detachment footwall under decreasing lithostatic pressure (Andreani et al., 2007). The continuity of some of these veins (e.g., banded veins) over length scales higher than the drilled or dredged sample size however precludes accurate characterization and quantification of the permeability they represent. In contrast, fractures only partially account for the development of the mesh texture or serpentine 2 recrystallization that rather resemble alteration halos along thin and unfilled central fractures. In both cases, the reaction front (olivine-lizardite or lizardite-chrysotile) progressively moves away from

Table 3
Comparison between serpentine separates (Rouméjon et al., 2015) and in-situ measurements in the SWIR samples.

Sample	Textures in serpentine separates	$\delta^{18}O$ (‰)	In situ textures	Average $\delta^{18}O$ (‰)	Proportion (%)[a]	Reconstructed $\delta^{18}O$ (‰)	Difference
SMS-1	Fully serpentinized mesh texture	4	Inner mesh rims	3.44	64	2.93	
			Mesh cores	2.44	21		1.07
			Outer mesh rims	1.43	15		
	Banded vein + serpentine 2	3.4	Antigorite	2.44	20	–	
			Serpentine 2	2.52	20		–
			Banded vein	No data[b]	60		
SMS-2	Banded vein + antigorite	2.3	Antigorite	−2.15	30	–	–
			Banded vein	No data[b]	70		
SMS-3	Partially serpentinized mesh texture	4.8	Inner mesh rims	3.32	37 (41)[c]	2.18	
			Mesh cores	No data[b]	9		2.62
			Outer mesh rims	1.61	54 (59)[c]		
SMS-4	Partially serpentinized mesh texture	6	Mesh rims	2.61	100	2.61	3.39
SMS-5	Fully serpentinized mesh texture	4.6	Mesh rims	4.12	58	3.67	0.93
			Mesh cores	3.04	42		
	Serpentine 2	1.9	Serpentine 2	−0.29	100	−0.29	2.19

The precision is ±0.2‰ for serpentine separates $\delta^{18}O$ values and around ±0.8‰ for reconstructed $\delta^{18}O$ values.
[a] relative proportions calculated on portions of SEM maps using the ImageJ software.
[b] textures no targeted with SHRIMP or initially targeted with SHRIMP but giving unreliable data due to porosity.
[c] proportions recalculated without the mesh cores whose contribution is negligible (part of these 9% is olivine which was removed from the separates).

the fracture plane. To maintain on-going reactions, fluids must be channeled through the mesh rims or the serpentine 2, respectively, over a few hundred microns to a few millimeters. This is likely possible by the imperfect arrangement of lizardite plates as pseudo-columns in the mesh as observed in several contexts (Viti and Mellini, 1998; Boudier et al., 2010; see also Fig. 3a in Rouméjon et al., 2015) or by the reduced size and random orientation of the chrysotile fibers in serpentine 2 (see Fig. 3b in Rouméjon et al., 2015).

Although all serpentine textures are porous/permeable, the absence of correlation between the $\delta^{18}O$ value and the total oxide content in most of our SHRIMP targets (Fig. 2) suggests that porosity does not massively influence the $\delta^{18}O$. We thus consider that the relative $\delta^{18}O$ variations between these textures are real and are discussed below. In the following, we attempt to translate the $\delta^{18}O$ values into temperatures and water-rock ratios. Knowing that in-situ measurements give lower $\delta^{18}O$ values than traditional bulk rock analyses, these estimates will likely correspond to overestimated values compared to previously published data. In contrast, the textures associated with the discarded $\delta^{18}O$ data reflect a much higher porosity, as suggested by the correlation between the decreasing $\delta^{18}O$ and the decreasing total oxide content, and by observations on SEM images. Some correspond to the imperfect arrangement of chrysotile fibers in fibrous veins. Others are mesh cores (samples 69A-6 and SMS-3) or serpentine 2 and banded veins (sample SMS-2) and probably indicate dissolution of a phase, maybe part of the serpentine or early brucite (Jöns et al., 2017).

6.2. Temperatures of serpentinization and time-integrated water-rock ratios

The fractionation of oxygen isotopes between serpentine and the fluid is a function of the temperature so that several geothermometers have been proposed over the past decades (Früh-Green et al., 1996; Saccocia et al., 2009; Wenner and Taylor, 1971; Zheng, 1993). Here we consider the most recent calibration of Saccocia et al. (2009), obtained experimentally by reacting lizardite and chrysotile with water at 250–450 °C. The time-integrated water-rock ratio (hereafter simply referred to as water-rock ratio) is the total amount of water that interacted with a volume of rock during the fluid-rock interaction history. For a given temperature, the fractionation evolves with increasing water-rock ratio until equilibrium at a given temperature is reached. Conversely, one can calculate the water-rock ratio assuming the composition of the initial fluid, mineral reactant and mineral product, and a crystallization temperature (Taylor, 1977), either in a closed system (every particle of fluid undergoes recirculation and progressive homogenization with the rock) or in an open system (every particle of fluid makes one single pass through the rock).

Using the geothermometer of Saccocia et al. (2009), the $\delta^{18}O$ of serpentine minerals measured in our samples correspond to temperatures mostly between 210 and 350 °C for a seawater-dominated fluid ($\delta^{18}O$ = 0–0.1‰; e.g., Lost City vent field; Früh-Green et al., 2004; Fig. 8a) and between 250 and 450 °C assuming hydrothermally altered seawater ($\delta^{18}O$ = 2.4‰; e.g., Snake Pit vent field, MAR 23°N; Campbell et al., 1988; Fig. 8b). Samples from the Atlantis Massif and the SWIR share similar ranges of calculated temperatures and no distinction can be made between samples.

At SWIR, the $\delta^{18}O$ values of serpentine separates decrease with the serpentinization sequence (Rouméjon et al., 2015), which was interpreted as a record of an increasing water-rock ratio (< 1 for the mesh texture and > 1 for the subsequent recrystallizations and veins) under nearly constant temperatures (270–340 °C), assuming a fluid with a constant isotopic composition. Here, we observe a comparable decrease in $\delta^{18}O$ at the sample scale, both at SWIR and Atlantis Massif. The data are consistent with the interpretation that the serpentinization textures form at nearly constant temperatures and increasing water-rock ratio, given that the formation of mesh textures is recognized to start at very low water-rock ratios (e.g., Viti and Mellini, 1998) while

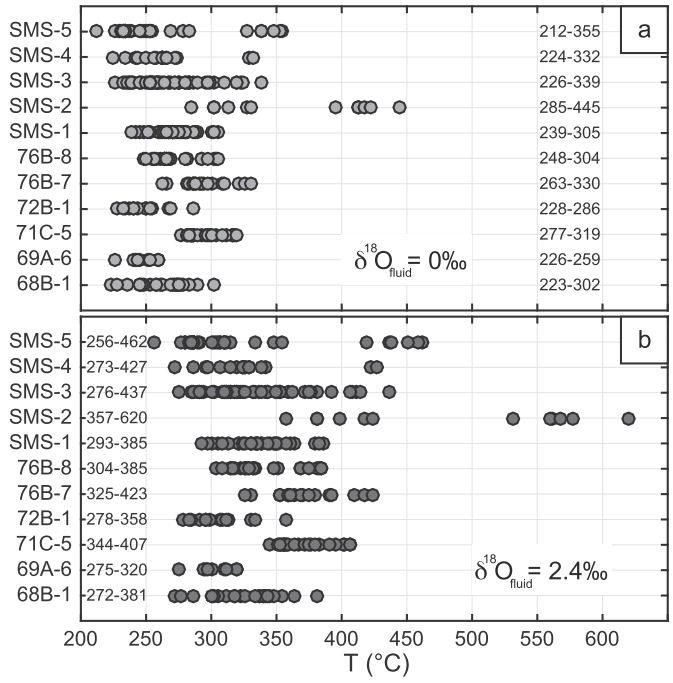

Fig. 8. Temperatures of serpentine crystallization calculated using the oxygen isotope geothermometer of Saccocia et al. (2009). The upper panel is for seawater-type fluids ($\delta^{18}O$ = 0‰), the lower panel is for more hydrothermally altered seawater ($\delta^{18}O$ = 2.4‰). The reported values are the minimum and maximum temperatures for each sample.

veins are, by definition, associated with high water-rock ratios. In addition, the development of veins also marks a transition towards shallower and more open conditions during exhumation (Andreani et al., 2007). This could imply an increasing influence of colder seawater with light composition and therefore seems incompatible with a temperature increase. Using this framework, we now focus on the texture scale to characterize local fluid-rock processes and propose more accurate estimates of serpentinization temperatures and associated water-rock ratios.

6.3. Inputs from in-situ measurements on local fluid-rock interaction

6.3.1. Olivine

Oxygen isotope compositions of primary olivine in peridotites generally range from 4.8 to 5.9‰, with an average $\delta^{18}O$ of ~5.2‰ (Eiler et al., 2011; Mattey et al., 1994). Studies of individual grains in multiple samples have revealed an inter- and intracrystalline variability lower than 1‰ suggesting that the upper mantle is relatively homogeneous (Eiler, 2001; Eiler et al., 2011; Mattey et al., 1994). These results are independent of the facies (spinel-, garnet-, or diamond-bearing peridotites; Mattey et al., 1994), mantle metasomatism (anhydrous versus hydrous, i.e. amphibole-bearing peridotite; Chazot et al., 1997), or the degree of partial melting (Eiler, 2001). Mattey et al. (1994) also reported an average $\delta^{18}O$ of ~5.6‰ for orthopyroxenes and ~5.7‰ for clinopyroxenes and estimated an average $\delta^{18}O$ of 5.5‰ for peridotites. Our results are in agreement with these values: with the exception of one sample, the olivine grains have an average $\delta^{18}O$ of 5.1 to 5.6‰ with intracrystalline variability of maximum 0.9‰. This suggests a relative homogeneity of the protolith so that any variability in serpentine textures derives from hydrothermal processes and heterogeneous fluid-rock interaction.

6.3.2. Mesh texture: onset and developments

In the partially serpentinized domains of the mesh textures, the narrowest and magnetite-free mesh rims record the highest $\delta^{18}O$ values

(up to 4.6–4.7‰). In contrast, the largest and magnetite-bearing textures have the lightest compositions (down to 2.2‰; Fig. 5a and b) and equal the values observed in the fully serpentinized domains (2–2.5‰). This suggests: 1) that mesh rims have relatively high $\delta^{18}O$ values when they form after olivine with $\delta^{18}O$ decreasing with increasing fluid-rock interaction and serpentinization, and 2) fluid-rock interaction is heterogeneous at the mesh cell scale (100–200 μm).

The onset of mesh texture formation has been proposed to occur at very low water-rock ratios (Viti and Mellini, 1998). We can test this hypothesis by calculating the $\delta^{18}O$ of serpentine that would be obtained by serpentinizing a harzburgite under stoichiometric conditions, i.e. all the water is consumed, in a closed-system case. We consider the following reaction:

$$\text{Olivine} + \text{Orthopyroxene} + 2H_2O = \text{Serpentine}.$$

And the mass-balance equation described in Taylor (1977):

$$W\delta^{18}O_{fluid}^{initial} + R\delta^{18}O_{rock}^{initial} = W\delta^{18}O_{fluid}^{final} + R\delta^{18}O_{rock}^{final} \quad (1)$$

where W and R are the oxygen atomic proportions, respectively, of the fluid and the rock in the fluid+rock system. If all the water is consumed, Eq.(1) becomes:

$$W\delta^{18}O_{fluid} + R\delta^{18}O_{peridotite} = (W+R)\delta^{18}O_{serpentine} \quad (2)$$

So that:

$$\delta^{18}O_{serpentine} = \frac{{}^{W}/_{R}\,\delta^{18}O_{fluid} + \delta^{18}O_{peridotite}}{1 + {}^{W}/_{R}} \quad (3)$$

In our calculations, we use a water-rock ratio of 0.286 ($W/R = 2/7$), a $\delta^{18}O$ of 5.5‰ for the peridotite (Mattey et al., 1994) and of 0 and 2.4‰ for the fluid. The resulting serpentine has a $\delta^{18}O$ of 4.3–4.8‰, which matches the values measured in the narrow, magnetite-free, mesh rims and is consistent with the interpretation that the incipient serpentinization occurs under stoichiometric conditions. The heaviest $\delta^{18}O$ in the mesh texture therefore correspond to a weighted mixing of the mineral and fluid signatures. We acknowledge that the considered reaction with olivine and orthopyroxene may not be the most relevant for the investigated scales of reaction, especially during the early stages of serpentinization where orthopyroxene alteration could be delayed compared to olivine (e.g., Rouméjon et al., 2015). Alternatively, reaction of olivine alone with water can lead to serpentine associated with magnetite or brucite (e.g., Evans et al., 2013), requiring the consideration of the fractionation of oxygen isotopes between these products. However, magnetite and brucite bear negative $\delta^{18}O$ under comparable serpentinization conditions (e.g., Agrinier and Cannat, 1997; Saccocia et al., 1998) so that $\delta^{18}O$ in serpentine would be heavier than the calculated range, leading to similar conclusions.

The further decrease of $\delta^{18}O$ in the mesh rims correlates with continued progress of serpentinization. This is indicated by the increased width of the mesh rims, i.e. more olivine has been consumed, by the appearance of magnetite, whose production sharply increases after 75% serpentinization (Andreani et al., 2013a; Oufi et al., 2002), and by the compositions reaching similar $\delta^{18}O$ values as those measured in the fully serpentinized mesh textures. The heterogeneity of $\delta^{18}O$ within the mesh rims around single olivine relicts indicates that serpentinization does not proceed as efficiently in all directions at the mesh cell scale (100–200 μm; Fig. 5). The most likely explanation is that the fluid supply is heterogeneous so that fluids do not equally reach the reaction front around the olivine relict. At this scale of observation, fluid influx depends on how continuous and open the microfractures are and how well oriented they are compared to fluid flow. Some microfractures are therefore better suited to channel the fluids and serpentinization proceeds more efficiently along them (Rouméjon and Cannat, 2014). It follows that the mesh rims with the highest $\delta^{18}O$ represent relatively closed-system domains with limited fluid flux after the olivine to serpentine conversion, while the lightest compositions represent an evolved stage where $\delta^{18}O$ decreases because of increasing fluid-rock interaction.

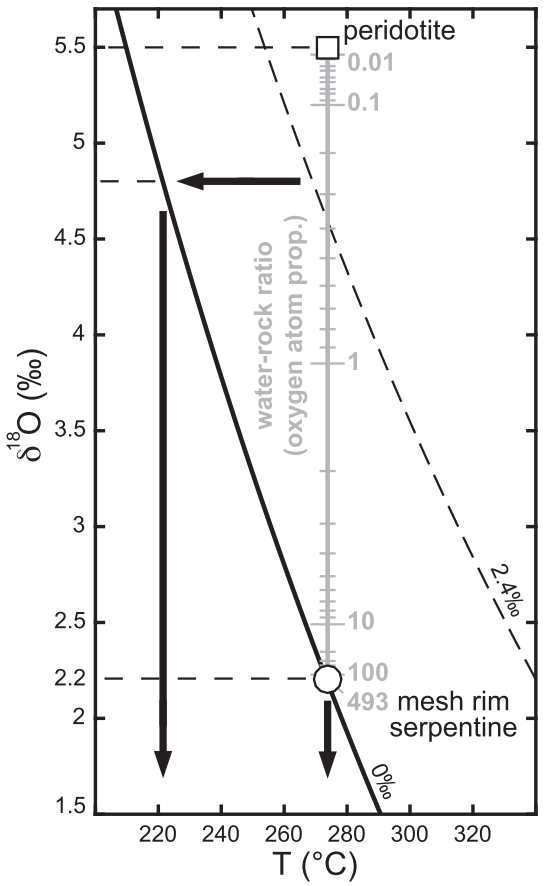

Fig. 9. Control of the time-integrated water-rock ratio on the evolution of oxygen isotope compositions in serpentine. In this example, the starting material has a $\delta^{18}O$ value of 5.5‰ and reacts with a fluid of 0‰ leading to a mesh rim with a $\delta^{18}O$ of 2.2‰. The fractionation corresponds to a temperature of ~275 °C (Saccocia et al., 2009) and to a water-rock ratio of ~493 (in oxygen atomic proportions, closed-system model; Taylor, 1977) or lower (30, see text). Considering an insufficient water-rock ratio and therefore a mesh rim with a heavier composition (e.g., 4.7‰) leads to underestimate the temperature (e.g., ~220 °C).

Such $\delta^{18}O$ decrease suggests that mesh rims require a significant water-rock ratio to approach the $\delta^{18}O$ value imposed by the temperature. In Fig. 9, we consider a transition from a peridotite (5.5‰) to a mesh rim (2.2‰) composition. The mesh rim $\delta^{18}O$ value corresponds to a temperature of ~275 °C for a fluid at 0‰ (~340 °C for a 2.4‰ fluid) and a water-rock ratio of ~493 using the non-stoichiometric case expressed by Eq.(1) in a closed system. The calculated ratio is very high and it is likely that the mesh rims do not reach full equilibrium $\delta^{18}O$ values imposed by the temperature. Considering that the rate of serpentine $\delta^{18}O$ decrease diminishes at ratios higher than 10, values approaching 2.2‰ could be reached at ratios one order of magnitude lower. For example, a $\delta^{18}O$ of 2.30‰ would correspond to a ratio of 30, i.e. 15 g of water for 1 g of rock when expressed in mass. This is on the same order than estimates of Andreani et al. (2013a) based on Fe redox state in fully serpentinized mesh textures (20 to 35 in mass, their Fig. 9a). Fig. 9 also shows that limited fluid fluxes maintain heavy serpentine $\delta^{18}O$, leading to colder temperatures estimates (e.g., 4.7‰ gives ~220 °C). In consequence, using mesh-textured peridotites to establish serpentinization temperatures could lead to underestimated temperatures, as at least some parts of the mesh texture interacted

with less fluids and may not achieve an equilibrium isotopic composition at a given temperature. Similarly, the bastites $\delta^{18}O$ values seem to decrease with on-going fluid-rock interaction: bastites associated with the mesh texture are heavier than those associated with antigorite or serpentine 2.

The fully serpentinized domains of the mesh textures reveal a different evolution in oxygen isotope exchange between Atlantis Massif and SWIR. At Atlantis Massif, mesh rims and mesh cores share similar $\delta^{18}O$ values in a given sample (Fig. 6a). This suggests that serpentinization occurred relatively fast, allowing a constant temperature and fluid composition and limiting the discrepancy of water-rock ratios between the mesh rims and mesh cores. In parallel, the samples can be divided in three groups based on the $\delta^{18}O$ values of the mesh rims: samples 69A-6 and 72B-1 are mostly above 2.5‰, samples 68B-1 and 71C-5 are mostly below, and sample 76B-8 is intermediate. The same division was previously established between the drill holes using textural observations and trace elements enrichment (Cu, U, Sr; Roumejon et al., 2018): Holes M0068B and M0071C correspond to portions of the detachment footwall that underwent long-lasting and intense fluid-rock interaction; Holes M0069A and M0072B underwent limited fluid-rock interaction; and Hole M0076B is intermediate with fluid-rock interaction becoming more intense later in the exhumation history. The $\delta^{18}O$ values therefore confirm that fluid fluxes and resulting fluid-rock interaction is spatially heterogeneous in the detachment footwall at Atlantis Massif, at scales of a few hundred meters to a kilometer. In contrast, at SWIR, the $\delta^{18}O$ of a given domain within the mesh texture is homogeneous between the samples (Fig. 6b): inner mesh rims are mostly above 2.5‰ while outer mesh rims are mostly below, and mesh cores are intermediate. Considering the chronology between these domains, the $\delta^{18}O$ decreases during the mesh texture formation. Again, this is most likely recording an increase in fluid-rock ratio so that serpentinization was probably slower at the SWIR than at Atlantis Massif although fluid-rock interaction was spatially homogeneous. Therefore, there appears to be a difference in the serpentinization style between the two locations that requires us to take into account the geological context. This is addressed in the last section of this discussion.

6.3.3. Serpentine recrystallization

Saccocia et al. (2009) quantified the amount of isotopic exchange between serpentine and water during different experimental runs. In their chrysotile experiments, the isotopic exchange was 6–10% at 250–350 °C respectively, while it ranged from 17 to 82% for their lizardite experiments at the same temperatures. These results correlate with the observation of partial conversion of lizardite to chrysotile via dissolution-recrystallization while chrysotile fibers morphology remained unchanged. This logically suggests that dissolution-recrystallization is more efficient than volume diffusion to equilibrate the serpentine minerals with the fluids. In a context of facilitated exchange with fluids, recrystallized textures (serpentine 2 chrysotile, antigorite) are more likely to reach equilibrium oxygen isotope compositions imposed by temperature than are mesh textures. This also explains the homogenization of $\delta^{18}O$ with the serpentinization sequence (Fig. 4c). It is therefore more appropriate to use $\delta^{18}O$ measured in the recrystallization textures to estimate serpentinization temperatures, and which yield temperatures between 259 and 289 °C (fluid at 0‰) and 319–362 °C (fluid at 2.4‰; Table 4). These estimates are in agreement with the observed mineralogical assemblages (serpentine ± magnetite after olivine). According to observations on natural samples, laboratory experiments, and thermodynamic models, iron is preferentially incorporated in magnetite rather than in Fe-rich serpentine and brucite at temperatures higher than 200 °C (Klein et al., 2009, 2014; Lafay et al., 2012; Malvoisin et al., 2012; Seyfried et al., 2007) and serpentinization of olivine remains efficient up to 350 °C (Allen and Seyfried, 2003; Malvoisin et al., 2012; Martin and Fyfe, 1970). These estimates also match previous analyses at Atlantis Massif, carried out on both serpentine separates (Früh-Green et al., 2004) and bulk rocks (Boschi et al., 2008; McCaig et al., 2010). The $\delta^{18}O$ range between 0.4 and 5.6‰ (one exception of 6.7‰) correspond to temperatures of 210–320 °C (seawater-dominated fluid) or 250–410 °C (hydrothermally altered seawater). As previously discussed, these temperatures may constitute overestimates due to the observed discrepancy with serpentine separates. We remain cautious with regard to the temperatures above 400 °C obtained on samples SMS-2 and SMS-5 as they are incompatible with the observed mineralogical assemblages.

Table 4
Temperatures of serpentinization using the oxygen isotope geothermometer of Saccocia et al. (2009) and the $\delta^{18}O$ values of serpentine 2 and antigorite textures in our samples.

Sample	Texture	$\delta^{18}O$ (‰)	T (°C) (fluid = 0‰)	T (°C) (fluid = 2.4‰)
71C-5	Antigorite	1.57	289	362
76B-7 + 8	Serpentine 2	1.68	286	358
76B-7	Antigorite	1.57	289	362
SMS-1	Antigorite	2.21	273	340
SMS-2	Antigorite	−2.15	417	568
SMS-4	Serpentine 2	2.86	259	319
SMS-5	Antigorite	−0.29	343	444

6.3.4. Banded veins

The depth of the serpentinization front remains unknown on-axis. It however reaches 4 km away from the detachment plane, based on off-axis seismic profiles that have been made in the Kane area (MAR, 23°N; Canales et al., 2000). The isotopic evolution of the down-going serpentinizing fluids as they reach this front is also unconstrained. The fact that these fluids penetrate and interact with several kilometers of variably altered peridotites and gabbros suggests that they do not maintain a typical seawater signature (0‰) at depth. Instead, they may be as high as 2.4‰ during the mesh and recrystallization textures formation, characterized by a rock-dominated and closed system environment, and probably constant temperatures. In contrast, later veins record a transition of the exhuming system towards more open and fluid-dominated conditions (Andreani et al., 2007) with increasing permeability and higher fluid fluxes. At these lesser depths, one can expect less hydrothermally altered seawater with lower $\delta^{18}O$ values and temperature.

We propose that the $\delta^{18}O$ decrease (Fig. 5e) coeval to the banded vein formation in samples 76B-7 and 76B-8 record such changing conditions, allowing us to evaluate which parameters trigger the decrease. The veins correspond to high water-rock ratios, we therefore assume that the crystallizing serpentine has equilibrated with the fluids. In Fig. 10, we represent the serpentine $\delta^{18}O$ as a function of temperature and $\delta^{18}O$ of the fluid. As previously argued, a progressive temperature increase during exhumation is unlikely and we consider maximum temperatures in the range of 335 to 370 °C to be most likely. A decrease from 1.4‰ down to 0‰, as observed in samples 76B-7 and 76B-8, is then framed by two end-member possibilities: 1) the fluids have the same temperature but have a lower $\delta^{18}O$, or 2) the fluids are colder and have a lower $\delta^{18}O$. Starting with a fluid of 1.4‰ implies a constant temperature. Note that this range of temperature, although probably overestimated, is in the range of hydrothermal fluids commonly measured in black-smoker systems (e.g., Douville et al., 2002). Finally, the value of 0.8‰ on the right side of the vein in Fig. 5e, is either attributed to another branch of the banded vein that open previously to the last bands of the main vein, or to a final stage of the same vein and could correspond to a pulse of warmer or higher $\delta^{18}O$, more hydrothermally altered seawater.

6.4. Influence of gabbro intrusions on fluid-rock interaction at Atlantis Massif and SWIR 62–65°E

In this study, we show on the basis of isotopic and major element chemical arguments that despite similar textural sequences, serpentinization proceeds differently in peridotites exhumed at the

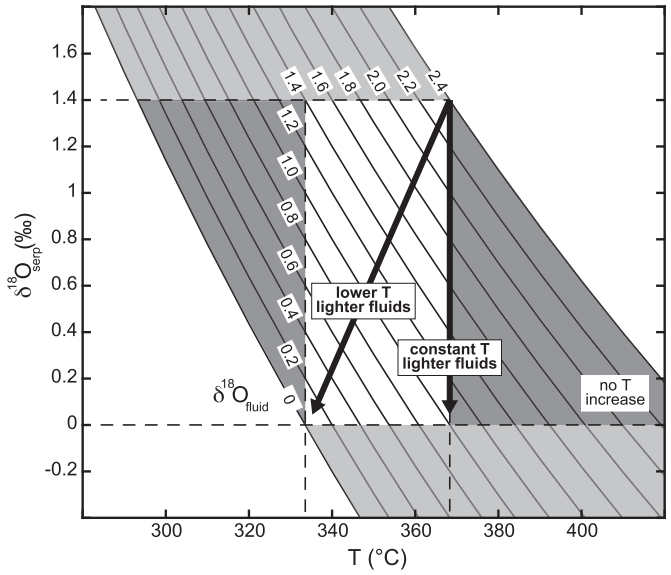

Fig. 10. Evolution of temperature and $\delta^{18}O$ of the fluid to explain the decrease of the serpentine $\delta^{18}O$ measured in the banded vein of samples 76B-7 and 76B-8. The serpentine $\delta^{18}O$ decreases from 1.4 to 0.1‰ (limited by the light grey fields) without an increase in temperature (limited by the darker grey fields). The two possibilities to explain the $\delta^{18}O$ decrease are: 1) the fluids have the same temperature but become progressively isotopically lighter, or 2) the fluids are progressively colder and isotopically lighter. Note that the considered temperatures are within the range of what is measured in hydrothermal fluids escaping black-smoker-type vents.

Atlantis Massif and along the easternmost SWIR (62–65°E). At Atlantis Massif, the mesh texture development occurs relatively fast and fluid-rock interaction is spatially heterogeneous in the detachment footwall (Fig. 6), while the mesh texture development is slower and fluid-rock interaction is spatially homogeneous at SWIR. Serpentine textures in the SWIR samples are systematically enriched in Al compared to those at Atlantis Massif and show a Si enrichment between the mesh texture formation and the subsequent recrystallizations and veins (Fig. 7). At Atlantis Massif, only samples from Site M0071, associated with intense fluid-rock interaction and small amounts of altered gabbros (Rouméjon et al., 2018), are enriched in Al. The highest Si enrichments in serpentine textures correlate with the presence of talc after the mesh texture in Hole M0068B samples and after serpentine 2 in Hole M0076B samples, two holes associated with intense fluid-rock interaction and a relative proximity with altered gabbros (Früh-Green et al., 2017). Samples from Holes M0069A and M0072B show only a limited Si enrichment between the mesh texture and the subsequent recrystallizations and veins. They are associated with portions of the holes that underwent limited fluid-rock interaction and respectively no and significant amounts of altered gabbros.

The average spreading rate at Atlantis Massif (24 mm.yr^{-1}; Zervas et al., 1995) is higher than at SWIR (14 mm.yr^{-1}; Patriat et al., 2008). This implies a faster exhumation at Atlantis Massif so that one could expect that alteration conditions (e.g., temperature, system openness) evolve faster and lead to significant $\delta^{18}O$ changes among textures. As this is not the case (e.g., Figs. 4 or 6a), we conclude that the spreading rates are slow enough not to influence the course of serpentinization. Instead, gabbros account for 30% of the peridotite-gabbro volume exhumed at Atlantis Massif (Blackman et al., 2002; Früh-Green et al., 2017; Karson et al., 2006) compared to 3% at the SWIR (Sauter et al., 2013). Although the distribution and size of these gabbroic bodies remain unconstrained, these proportions could explain the observed isotopic and compositional discrepancies.

Gabbros, which intruded into the peridotite before hydration commenced, likely act as relatively impermeable domains, because pyroxenes and plagioclases are generally less fractured than the olivine. Olivine grains are crosscut by tight and regularly-spaced microfractures, providing an efficient permeability network to channel hydrothermal fluids through the peridotite (Rouméjon and Cannat, 2014). In the geological model presented in Fig. 11, we therefore tentatively propose that a limited amount of gabbros, such as at SWIR, only slightly influences fluid flow paths. This allows a uniform distribution of seawater-derived fluids into the peridotite (Fig. 11, left panel) and explains the homogeneity of the $\delta^{18}O$ values acquired in the mesh texture. Higher volumes of gabbros, as observed at Atlantis Massif, may provide hindrances to the fluid flow path and variably influence fluid-rock interaction and isotopic exchange along its path. The gabbroic bodies likely concentrate fluid flow in intermediate domains (Fig. 11, right panel), leading to intense, focused fluid-rock interaction and isotopic exchange (i.e. low $\delta^{18}O$) in the mesh textures, such as at Site M0071 and Holes M0068B and M0076B, while they shield other domains leading to less intense fluid-rock interaction (i.e. higher $\delta^{18}O$) in the mesh textures, evident in Hole M0069A. In Hole M0072B, the selected sample corresponds to a domain (tens of centimeter in size) overprinted by fracturing during mesh texture emplacement. These fractures channeled the fluids so that the mesh texture underwent only limited fluid-rock interaction (Rouméjon et al., 2018).

Part of the fluids nevertheless penetrates the gabbros and the pyroxenes of the peridotites. Their alteration releases Ca, Si, and Al that form tremolite, talc, and chlorite in-situ, or are transported into the serpentinized peridotites (e.g., Boschi et al., 2006). If transported, Ca is carried away by the fluids because its ionic radius is too large to allow incorporation in serpentine (Shannon, 1976). The ubiquitous presence of serpentine ± magnetite and absence of brucite in the studied samples, including in domains associated with very low water-rock ratios, suggests a moderate external input of $SiO_{2(aq)}$ during olivine serpentinization and mesh texture emplacement (e.g., Frost and Beard, 2007). Given the delayed alteration of pyroxenes, especially at SWIR (Rouméjon et al., 2015), an internal source of $SiO_{2(aq)}$ is less likely. The subsequent Si-enrichment observed in some samples (Fig. 7) probably derives from submicrometric intergrowths of phases enriched in Si compared to lizardite/chrysotile, such as antigorite or talc. These intergrowths must however be limited, as limited departure from stoichiometric serpentine compositions were measured and they could not be identified with micro-Raman spectroscopy. External addition of Si to serpentine is clearly identified in Hole M0068B drilled at Atlantis Massif. Talc progresses from an altered gabbro into the serpentinized harzburgite where it replaces serpentine, indicating Si mobility over almost a meter (Rouméjon et al., 2018; e.g., Core M0068B-2R1 in their Fig. 3). With distance to the gabbroic source, the $SiO_{2(aq)}$ content of the fluids progressively decreases and only allows traces of Si-rich phases to locally crystallize in the serpentine textures (e.g., in sample 68B-1). In contrast, even with mafic intrusions in the vicinity, the mesh texture from Hole M0072B is not enriched in Si because the fluid access to the serpentine textures became limited after the early hydration phase (Rouméjon et al., 2018). The enrichment observed between the mesh texture and the subsequent recrystallizations and veins is due to late Si arrival, either because the altered gabbros are further away (Holes M0069A and M0076B, and possibly Site M0071) and/or because pyroxene alteration was delayed (SWIR; Rouméjon et al., 2015).

The decoupling of Si and Al enrichments seems then paradoxical but can be explained by the influence of pH on Al mobility. We calculated the activity of simple aqueous Al species considering corundum and using the Deep Earth Water Model program (Sverjensky et al., 2014) and additional data from Shock et al. (1997). The activity of individual Al species and their total are presented in Fig. 12 as a function of pH at 1 kbar and 300 °C. Al mobility is the lowest around pH of 3 to 5 and increases at lower and higher pH. Serpentinization of peridotite has been shown to result in alkaline conditions (Palandri and Reed, 2004) so that the serpentinizing fluids reach pH of 9–11 at the Lost City vent field (Kelley et al., 2005) and up to 12 in springs issuing from serpentinites in the Oman ophiolite (e.g., Neal and Stanger, 1983). In contrast, fluids

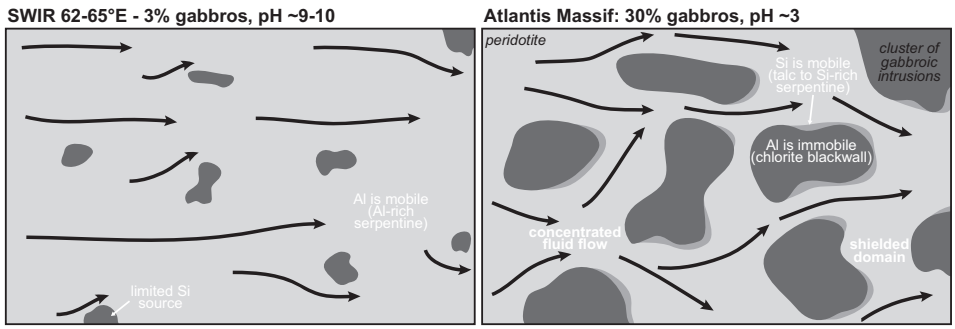

Fig. 11. Conceptual sketch illustrating how the abundance of gabbros, which are less permeable than the surrounding peridotite, influences fluid flow distribution. At SWIR (left), the low proportion of gabbros (3%) leads to a relatively homogeneous fluid distribution and to alkaline pH allowing Al mobility and incorporation in serpentine (see Fig. 12). At the Atlantis Massif (right), gabbros account for 30% so that fluids are concentrated in some domains while the gabbros shield other domains. Gabbros are also a source of Si and lead to locally acidic pH so that Al is immobile. The fluid flow direction is arbitrary.

interacting with gabbros or mafic lithologies become more acidic due to the dissolution of pyroxenes (Palandri and Reed, 2004) and to CO_2 released by melts (e.g., Alt, 1995). Fluids venting at the Rainbow, Logatchev, or Snake Pit fields have a pH around 3 (Douville et al., 2002). Thus, in the Atlantis Massif case, interaction between the serpentinizing fluids and the gabbros at depth likely led to locally acidic conditions (though the exact pH remains unconstrained) where Al is immobile and forms chlorite blackwalls at the contacts between gabbros and serpentinized peridotites (Früh-Green et al., 2017). At SWIR, the peridotite-dominated environment likely led to alkaline conditions allowing progressive loading of the fluids in Al after alteration of pyroxenes, spinels, and moderate amounts of gabbros. Al precipitates in serpentine when the activity becomes sufficiently high. It may reach levels allowing chlorite crystallization, as is locally observed (Rouméjon et al., 2015). Similar conditions probably occur at Atlantis Massif at Site M0071, where gabbros are rare. As for Si, limited fluid-rock interaction in Hole M0069A does not allow Al concentration and incorporation to serpentine, although gabbros are rare. Note that in order to keep this model simple, we have used corundum instead of a more complex mineralogical system so that the absolute activity values are admittedly overestimated.

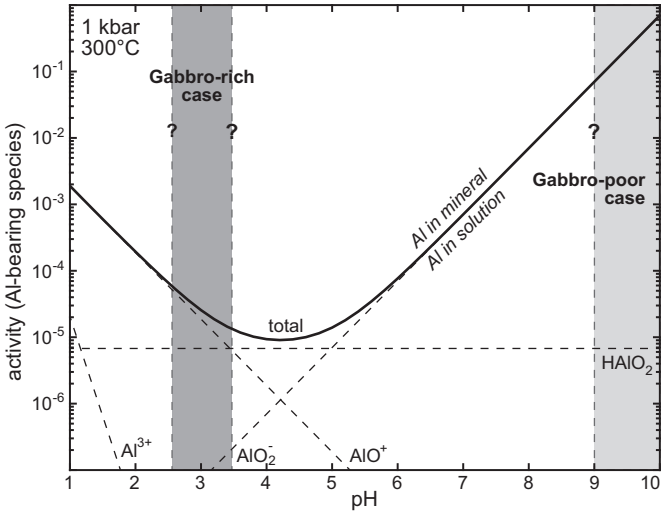

Fig. 12. Influence of the pH on aluminum activity at 1 kbar and 300 °C. Al mobility is the lowest around pH of 3–5, which could correspond to values reached in gabbro-rich environments. Mobility increases at lower pH or at higher pH, the latter corresponding to conditions associated with dominant serpentinization.

According to experimental studies, several factors could explain the difference in serpentinization rate in the mesh texture of the Atlantis Massif and SWIR samples.

However, our observations allow us to discard most of them. For instance, the effect of temperature of the serpentinization rate of olivine (Malvoisin et al., 2012; Martin and Fyfe, 1970; Wegner and Ernst, 1983) cannot be invoked, as temperatures appear to be similar at both locations. Similarly, the microfracturing network crosscutting the olivine have comparable and regular spacing so that the influence of the initial grain size (Malvoisin et al., 2012) can be dismissed. Aluminum has been shown to speed up the olivine to serpentine conversion (e.g., Andreani et al., 2013b), however, the highest enrichments in Al are in the SWIR samples serpentine textures that are associated with the slowest serpentinization rates. Finally, pH does not seem to play a role. Experiments under strongly alkaline conditions (Lafay et al., 2012) resulted in similar serpentinization rates as in earlier studies conducted at lower pH (Martin and Fyfe, 1970; Wegner and Ernst). More recently, McCollom et al. (2016) obtained lower rates, suggesting that alkaline conditions might increase the serpentinization rates. This however, contradicts our observations, with the slowest rates being associated with alkaline conditions. Instead, Lamadrid et al. (2017) recently conducted in-situ experiments to show that serpentinization rates increase when the salinity decreases (i.e. the water activity increases). Therefore, the renewal of the fluid supply by stronger fluid flow possibly helps to increase or at least maintain serpentinization rates. This could explain faster rates at Atlantis Massif where fluids may be channeled and concentrated in between the gabbroic bodies.

7. Conclusions

We measured in-situ oxygen isotope compositions in a sequence of serpentine textures in serpentinized harzburgites and dunites drilled at the Atlantis Massif (MAR, 30°N) and dredged along the easternmost SWIR (62–65°E). The sequence is similar at both locations and includes mesh textures after olivine and bastites after orthopyroxenes, recrystallization textures (chrysotile-dominated serpentine 2, and/or antigorite), and veins (fibrous, banded).These textures progressively formed during exhumation of the peridotites localized in the footwall of detachment faults.

In-situ analyses by SHRIMP proved to be porosity-dependent, which can be examined using the total oxide content measured by electron microprobe. They nevertheless give slightly lower $\delta^{18}O$ values than when analyzing bulk serpentine separates on the same samples.

At the sample scale, decreasing $\delta^{18}O$ values correlate with the textural sequence, which we argue is due to an increasing time-integrated water-rock ratio under a nearly constant temperature. Serpentinization linked to the initiation of mesh textures starts at stoichiometric water-rock ratios. Fluid supply subsequently increases but remains

heterogeneous at the mesh cell scale, creating heterogeneities in $\delta^{18}O$ at scales on the order of 100 μm. Some domains of the mesh texture are shielded from significant fluid flow during on-going serpentinization so that using mesh-textured samples to estimate serpentinization temperatures can lead to underestimated values. Instead, we consider the recrystallization textures and apply the geothermometer developed by Saccocia et al. (2009) to calculate temperatures on the order of 260–290 °C (seawater-dominated fluid) or 320–360 °C (hydrothermally altered seawater). The subsequent banded veins may record the evolution towards cooler and less altered, seawater-dominated fluids indicating interaction at shallower levels in the footwall as exhumation proceeds.

Finally, $\delta^{18}O$ values show that serpentinization may be faster at Atlantis Massif during mesh texture development, though laterally heterogeneous at scales of several hundred meters to a few kilometers, while it is slower and homogeneous at SWIR. We propose that the variations in oxygen isotope compositions reflects the varying volumes of gabbros intruded in the peridotite. At Atlantis Massif, a significant amount of gabbro influences the distribution of fluid flow in the footwall, leading to intense fluid-rock interaction favoring serpentinization in some domains while others remain shielded. The negligible amount of gabbros at SWIR allows a relatively homogeneous distribution of fluids. In addition, gabbro alteration leads to Si enrichment in the surrounding serpentine textures and to acidic pH that limit Al mobility. The relative absence of gabbros hinders Si enrichments but favors Al mobility and incorporation in serpentine.

Supplementary data to this article can be found online at https://doi.org/10.1016/j.lithos.2018.09.021.

Acknowledgements

We thank the captain and crew aboard the RRS James Cook as well as ECORD and the ESO staff for their efforts and support during all phases of IODP Expedition 357. Andreas Jallas and Suzanne Picazo are thanked for suggestions and help during sample preparation. Maria Rosa Scicchitano provided reference materials and helpful discussion regarding SHRIMP oxygen isotope analyses of serpentine. We thank Peter Holden for assistance when conducting analyses on SHRIMP and Lukas Martin and Matthieu Galvez for fruitful discussions. This manuscript benefited from constructive comments from two anonymous reviewers and editorial handling by M. Godard. We gratefully acknowledge funding by the Swiss National Science Foundation (SNF) project No. 200021_163187 and Swiss IODP, and contributions from Prof. Motohiko Murakami (Institute for Geochemistry and Petrology, ETH Zürich).

References

Agrinier, P., Cannat, M., 1997. Oxygen-isotope constraints on serpentinization processes in ultramafic rocks from the mid-Atlantic ridge (23°N). Proceedings of the Scientific Results 153, 381–388.

Ahn, I., Lee, J.I., Kusakabe, M., Choi, B.G., 2012. Oxygen isotope measurements of terrestrial silicates using a CO2-laser BrF5 fluorination technique and the slope of terrestrial fractionation line. Geosciences Journal 16, 7–16. https://doi.org/10.1007/s12303-012-0011-x.

Allen, D.E., Seyfried, W.E., 2003. Compositional controls on vent fluids from ultramafic-hosted hydrothermal systems at mid-ocean ridges: an experimental study at 400°C, 500 bars. Geochimica et Cosmochimica Acta 67, 1531–1542. https://doi.org/10.1016/S0016-7037(02)01173-0.

Andreani, M., Baronnet, A., Boullier, A.-M., Gratier, J.-P., 2004. A microstructural study of a "crack-seal" type serpentine vein using SEM and TEM techniques. European Journal of Mineralogy 16, 585–595. https://doi.org/10.1127/0935-1221/2004/0016-0585.

Andreani, M., Mevel, C., Boullier, A.-M., Escartín, J., 2007. Dynamic control on serpentine crystallization in veins: Constraints on hydration processes in oceanic peridotites. Geochemistry, Geophysics Geosystems 8. https://doi.org/10.1029/2006GC001373.

Andreani, M., Muñoz, M., Marcaillou, C., Delacour, A., 2013a. μXANES study of iron redox state in serpentine during oceanic serpentinization. Lithos 178, 70–83. https://doi.org/10.1016/j.lithos.2013.04.008.

Andreani, M., Daniel, I., Pollet-Villard, M., 2013b. Aluminum speeds up the hydrothermal alteration of olivine. American Mineralogist 98, 1738–1744.

Bach, W., Garrido, C.J., Paulick, H., Harvey, J., Rosner, M., 2004. Seawater-peridotite interactions: First insights from ODP Leg 209, MAR 15°N. Geochemistry, Geophysics Geosystems 5. https://doi.org/10.1029/2004GC000744.

Blackman, D.K., Cann, J.R., Janssen, B., Smith, D.K., 1998. Origin of extensional core complexes: evidence from the Mid-Atlantic Ridge at Atlantis Fracture Zone. Journal of Geophysical Research 103, 21315–21333. https://doi.org/10.1029/98JB01756.

Blackman, D.K., Karson, J.A., Kelley, D.S., Cann, J.R., Früh-Green, G.L., Gee, J.S., Hurst, S.D., John, B.E., Morgan, J., Nooner, S.L., Ross, D.K., Schroeder, T.J., Williams, E.A., 2002. Geology of the Atlantis Massif (Mid-Atlantic Ridge, 30°N): Implications for the evolution of an ultramafic oceanic core complex. Marine Geophysical Researches 23, 443–469. https://doi.org/10.1023/B:MARI.0000018232.14085.75.

Blackman, D.K., Ildefonse, B., John, B.E., Ohara, Y., Miller, D.J., MacLeod, C.J., Expedition 304/305 Scientists, 2006. Proceedings of the Integrated Ocean Drilling Program. Texas, Integrated Ocean Drilling Program Manage- ment International, Inc., College Station https://doi.org/10.2204/iodp. proc.304305.2006.

Boschi, C., Früh-Green, G.L., Delacour, A., Karson, J.A., Kelley, D.S., 2006. Mass transfer and fluid flow during detachment faulting and development of an oceanic core complex, Atlantis Massif (MAR 30°N). Geochemistry, Geophysics Geosystems 7. https://doi.org/10.1029/2005GC001074.

Boschi, C., Dini, A., Früh-Green, G.L., Kelley, D.S., 2008. Isotopic and element exchange during serpentinization and metasomatism at the Atlantis Massif (MAR 30°N): Insights from B and Sr isotope data. Geochimica et Cosmochimica Acta 72, 1801–1823. https://doi.org/10.1016/j.gca.2008.01.013.

Boudier, F., Baronnet, A., Mainprice, D., 2010. Serpentine Mineral Replacements of Natural Olivine and their Seismic Implications: Oceanic Lizardite versus Subduction-Related Antigorite. Journal of Petrology 51, 495–512. https://doi.org/10.1093/petrology/egp049.

Canales, J.P., Collins, J.A., Escartín, J., Detrick, R.S., 2000. Seismic structure across the rift valley of the Mid-Atlantic Ridge at 23°20′ (MARK area): Implications for crustal accretion processes at slow spreading ridges. Journal of Geophysical Research 105, 28411–28425.

Cann, J., Blackman, D.K., Smith, D.K., McAllister, E., Janssen, B., Mello, S., Avgerinos, E., Pascoe, A.R., Escartín, J., 1997. Corrugated slip surfaces formed at ridge-transform intersections on the Mid-Atlantic Ridge. Nature 385, 329–332.

Cannat, M., 1993. Emplacement of Mantle Rocks in the Seafloor at Mid-Ocean Ridges. Journal of Geophysical Research 98, 4163–4172.

Cannat, M., Rommevaux-Jestin, C., Sauter, D., Deplus, C., Mendel, V., 1999. Formation of the axial relief at the very slow spreading Southwest Indian Ridge (49 to 69 E). Journal of Geophysical Research 104, 22825–22843.

Cannat, M., Sauter, D., Mendel, V., Ruellan, E., Okino, K., Escartín, J., Combier, V., Baala, M., 2006. Modes of seafloor generation at a melt-poor ultraslow-spreading ridge. Geology 34, 605–608. https://doi.org/10.1130/G22486.1.

Cannat, M., Agrinier, P., Bickert, M., Brunelli, D., Hamelin, C., Lecoeuvre, A., Onstad, S.L., Maia, M., Prampolini, M., Rouméjon, S., Vitale Brovarone, A., Besançon, S., Assaoui, E., 2017. Mid Ocean Ridge processes at very low melt supply: Submersible exploration of smooth ultramafic seafloor at the Southwest Indian Ridge, 64°E. American Geophysical Union Fall Meeting.

Chazot, G., Lowry, D., Menzies, M., Mattey, D., 1997. Oxygen isotopic composition of hydrous and anhydrous mantle peridotites. Geochimica et Cosmochimica Acta 61, 161–169. https://doi.org/10.1016/S0016-7037(96)00314-6.

Delacour, A., Früh-Green, G.L., Frank, M., Gutjahr, M., Kelley, D.S., 2008. Sr- and Nd-isotope geochemistry of the Atlantis Massif (30°N, MAR): Implications for fluid fluxes and lithospheric heterogeneity. Chemical Geology 254, 19–35. https://doi.org/10.1016/j.chemgeo.2008.05.018.

Dick, H.J.B., Lin, J., Schouten, H., 2003. An ultraslow-spreading class of ocean ridge. Nature 426, 405–412. https://doi.org/10.1038/nature02128.

Douville, E., Charlou, J.-L., Oelkers, E.H., Bienvenu, P., Colon, C.F.J., Donval, J.-P., Fouquet, Y., Prieur, D., Appriou, P., 2002. The rainbow vent fluids (36°14′N, MAR): the influence of ultramafic rocks and phase separation on trace metal content in Mid-Atlantic Ridge hydrothermal fluids. Chemical Geology 184, 37–48.

Eiler, J.M., 2001. Oxygen Isotope Variations of Basaltic Lavas and Upper Mantle Rocks. Rev. Mineral. Geochemistry 43, 319–364. https://doi.org/10.2138/gsrmg.43.1.319.

Eiler, J., Stolper, E.M., McCanta, M.C., 2011. Intra- and Intercrystalline Oxygen Isotope Variations in Minerals from Basalts and Peridotites. Journal of Petrology 52, 1393–1413. https://doi.org/10.1093/petrology/egr006.

Evans, B.W., Hattori, K., Baronnet, A., 2013. Serpentinite: what, why, where? Elements 9, 99–106. https://doi.org/10.2113/gselements.9.2.99.

Falcon-Suarez, I., Bayrakci, G., Minshull, T.A., North, L.J., Best, A.I., Rouméjon, S., Party, I.E., 2017. Elastic and electrical properties and permeability of serpentinites from Atlantis Massif, Mid-Atlantic Ridge. Geophysical Journal International 211, 708–721. https://doi.org/10.1093/restud/rdx027.

Frost, B.R., Beard, J.S., 2007. On silica activity and serpentinization. Journal of Petrology 48 (7), 1351–1368.

Früh-Green, G.L., Plas, A., Lécuyer, C., 1996. Petrologic and stable isotope constraints on hydrothermal alteration and serpentinization of the epr shallow mantle at hess deep (site 895). Proceedings of the Ocean Drill Program Science Results 147, 255–291.

Früh-Green, G.L., Kelley, D.S., Bernasconi, S.M., Karson, J.A., Ludwig, K.A., Butterfield, D.A., Boschi, C., Proskurowski, G., 2003. 30,000 years of Hydrothermal activity at the lost City Vent Field. Science 80 (301), 495–498.

Früh-Green, G.L., Connolly, J.A.D., Plas, A., Kelley, D.S., Grobety, B., Wilcock, W.S.D., 2004. Serpentinization of oceanic peridotites: implications for geochemical cycles and biological activity the Subseafloor biosphere at mid-ocean ridges. In: DeLong, E.F., Kelley, D.S., Baross, J.A., Craig Cary, S. (Eds.), The Subseafloor Biosphere at Mid-Ocean Ridges. AGU, pp. 119–136.

Früh-Green, G.L., Orcutt, B.N., Green, S.L., Cotterill, C., Morgan, S., Akizawa, N., Bayrakci, G., Behrmann, J.-H., Boschi, C., Brazleton, W.J., Cannat, M., Dunkel, K.G., Escartin, J., Harris, M., Herrero-Bervera, E., Hesse, K., John, B.E., Lang, S.Q., Lilley, M.D., Liu, H.Q., Mayhew, L.E., McCaig, A.M., Menez, B., Morono, Y., Quéméneur, M., Rouméjon, S., Sandaruwan

Ratnayake, A., Schrenk, M.O., Schwarzenbach, E.M., Twing, K.I., Weis, D., Whattham, S. A., Williams, M., and Zhao, R., 2017. Expedition 357 summary. In Früh-Green, G.L., Orcutt, B.N., Green, S.L., Cotterill, C., and the Expedition 357 Scientists, Atlantis Massif Serpentinization and Life, Proceedings of the International Ocean Discovery Program College Station, TX International Ocean Discovery Program). 10.14379/iodp.proc.357.101.2017

Früh-Green, G.L., Orcutt, B.N., Rouméjon, S., Lilley, M.D., Morono, Y., Green, S., Cotterill, C., Expedition 357 Scientists, 2018. Magmatism, serpentinization and life: Insights through drilling the Atlantis Massif (IODP Expedition 357). Lithos https://doi.org/10.1016/j.lithos.2018.09.012.

Grauby, O., Baronnet, A., Devouard, B., Schoumacker, K., Demirdjian, L., 1998. The chrysotile–polygonal serpentine– lizardite suite synthesized from a 3 MgO–2 SiO2–excess H2O gel. Terra Nova 1, 24.

Ickert, R.B., Hiess, J., Williams, I.S., Holden, P., Ireland, T.R., Lanc, P., Schram, N., Foster, J.J., Clement, S.W., 2008. Determining high precision, in situ, oxygen isotope ratios with a SHRIMP II: analyses of MPI-DING silicate-glass reference materials and zircon from contrasting granites. Chemical Geology 257, 114–128. https://doi.org/10.1016/j.chemgeo.2008.08.024.

Ildefonse, B., Blackman, D.K., John, B.E., Ohara, Y., Miller, D.J., MacLeod, C.J., Abe, N., Abratis, M., Andal, E.S., Andreani, M., Awaji, S., Beard, J.S., Brunelli, D., Charney, A.B., Christie, D.M., Delacour, A., Delius, H., Drouin, M., Einaudi, F., Escartin, J., Frost, B.R., Fryer, P.B., Gee, J.S., Godard, M., Grimes, C.B., Halfpenny, A., Hansen, H.E., Harris, A.C., Hayman, N.W., Hellebrand, E., Hirose, T., Hirth, J.G., Ishimaru, S., Johnson, K.T.M., Karner, G.D., Linek, M., Maeda, J., Mason, O.U., McCaig, A.M., Michibayashi, K., Morris, A., Nakagawa, T., Nozaka, T., Rosner, M., Searle, R.C., Suhr, G., Tamura, A., Tominaga, M., von der Handt, A., Yamasaki, T., Zhao, X., 2007. Oceanic core complexes and crustal accretion at slow-speading ridges. Geology 35, 623–626. https://doi.org/10.1130/G23531A.1.

Jamtveit, B., Putnis, C.V., Malthe-Sørenssen, A., 2009. Reaction induced fracturing during replacement processes. Contrib. Mineral. Petrol. 157, 127–133. https://doi.org/10.1007/s00410-008-0324-y.

Jöns, N., Kahl, W.-A., Bach, W., 2017. Reaction-induced porosity and onset of carbonation in abyssal peridotites: insights from 3D high-resolution microtomography. Lithos 268–271, 274–284. https://doi.org/10.1016/j.lithos.2016.11.014.

Kahl, W.-A., Jöns, N., Bach, W., Klein, F., Alt, J.C., 2015. Ultramafic clasts from the South Chamorro serpentine mud volcano reveal a polyphase serpentinization history of the Mariana forearc mantle. Lithos 227, 99–147. https://doi.org/10.1016/j.lithos.2015.03.015.

Karson, J.a., Thompson, G., Humphris, S.E., Edmond, J.M., Bryan, W.B., Brown, J.R., Winters, A.T., Pockalny, R.A., Casey, J.F., Campbell, A.C., Klinkhammer, G., Palmer, M.R., Kinzler, R.J., Sulanowska, M.M., 1987. Along-axis variations in seafloor spreading in the MARK area. Nature 328, 681–685. https://doi.org/10.1038/328681a0.

Karson, J.A., Früh-Green, G.L., Kelley, D.S., Williams, E.A., Yoerger, D.R., Jakuba, M., 2006. Detachment shear zone of the Atlantis Massif core complex, Mid-Atlantic Ridge, 30°N. Geochemistry, Geophysics Geosystems 7. https://doi.org/10.1029/2005GC001109.

Kelemen, P.B., Kikawa, E., Miller, D.J., Shipboard Scientific Party of ODP Leg 209, 2004. Proceedings of the Ocean Drilling Program Initial Reports, 209. Ocean Drilling Program, College Station, TX.

Kelley, D.S., Shank, T.M., 2010. Hydrothermal systems: a decade of discovery in slow spreading environments. Geophysics Monograph Series 188, 369–407. https://doi.org/10.1029/2010GM000945.

Kelley, D.S., Karson, J.A., Blackman, D.K., Früh-Green, G.L., Butterfield, D.A., Lilley, M.D., Olson, E.J., Schrenk, M.O., Roe, K.K., Lebon, G.T., Rivizzigno, P., AT3-60, SP, 2001. An off-axis hydrothermal vent field near the Mid-Atlantic Ridge at 30°N. Nature 412, 145–149. https://doi.org/10.1038/35084000.

Kelley, D.S., Karson, J.A., Früh-Green, G.L., Yoerger, D.R., Shank, T.M., Butterfield, D.A., Hayes, J.M., Schrenk, M.O., Olson, E.J., Proskurowski, G., Jakuba, M., Bradley, A.S., Larson, B., Ludwig, K., Glickson, D., Buckman, K., Bradley, A.S., Brazelton, W.J., Roe, K.K., Bernasconi, S.M., Elend, M.J., Lilley, M.D., Baross, J.A., Summons, R.E., Sylva, S.P., 2005. A Serpentinite-Hosted Ecosystem: the lost City Hydrothermal Field. Science 80 (307), 1428–1434.

Kita, N.T., Ushikubo, T., Fu, B., Valley, J.W., 2009. High precision SIMS oxygen isotope analysis and the effect of sample topography. Chemical Geology 264, 43–57. https://doi.org/10.1016/j.chemgeo.2009.02.012.

Klein, F., Bach, W., Jöns, N., McCollom, T., Moskowitz, B., Berquó, T., 2009. Iron partitioning and hydrogen generation during serpentinization of abyssal peridotites from 15°N on the Mid-Atlantic Ridge. Geochimica et Cosmochimica Acta 73, 6868–6893. https://doi.org/10.1016/j.gca.2009.08.021.

Klein, F., Bach, W., Humphris, S.E., Kahl, W.-A., Jöns, N., Moskowitz, B., Berquo, T.S., 2014. Magnetite in seafloor serpentinite-Some like it hot. Geology 42, 135–138. https://doi.org/10.1130/G35068.1.

Lafay, R., Montes-Hernandez, G., Janots, E., Chiriac, R., Findling, N., Toche, F., 2012. Mineral replacement rate of olivine by chrysotile and brucite under high alkaline conditions. Journal of Crystal Growth 347, 62–72. https://doi.org/10.1016/j.jcrysgro.2012.02.040.

Lamadrid, H.M., Rimstidt, J.D., Schwarzenbach, E.M., Klein, F., Ulrich, S., Dolocan, A., Bodnar, R.J., 2017. Effect of water activity on rates of serpentinization of olivine. Nature Communications 8, 16107. https://doi.org/10.1038/ncomms16107.

Malvoisin, B., Brunet, F., Carlut, J., Rouméjon, S., Cannat, M., 2012. Serpentinization of oceanic peridotites: Kinetics and processes of San Carlos olivine hydrothermal alteration. Journal of Geophysical Results 117. https://doi.org/10.1029/2011JB008842.

Martin, B., Fyfe, W.S., 1970. Some experimental and theoretical observations on the kinetics of hydration reactions with particular reference to serpentinization. Chemical Geology 6, 185–202.

Mattey, D., Lowry, D., Macpherson, C., 1994. Oxygen isotope composition of mantle peridotite. Earth and Planetary Science Letters 128, 231–241. https://doi.org/10.1016/0012-821X(94)90147-3.

McCaig, A.M., Delacour, A., Fallick, A.E., Castelain, T., Früh-Green, G.L., 2010. Detachment Fault Control on Hydrothermal Circulation Systems : Interpreting the Subsurface beneath the TAG Hydrothermal Field using the Isotopic and Geological Evolution of Oceanic Core Complexes in the Atlantic. Geophysics Monograph Series 188, 207–239.

McCollom, T.M., Klein, F., Robbins, M., Moskowitz, B., Berquó, T.S., Jöns, N., Bach, W., Templeton, A., 2016. Temperature trends for reaction rates, hydrogen generation, and partitioning of iron during experimental serpentinization of olivine. Geochimica et Cosmochimica Acta 181, 175–200. https://doi.org/10.1016/j.gca.2016.03.002.

Michael, P.J., Langmuir, C.H., Dick, H.J.B., Snow, J.E., Goldstein, S.L., Graham, D.W., Lehnert, K., Kurras, G., Jokat, W., Mühe, R., Edmonds, H.N., 2003. Magmatic and amagmatic seafloor generation at the ultraslow-spreading Gakkel ridge, Arctic Ocean. Nature 423, 956–961. https://doi.org/10.1038/nature01704.

Miller, D.J., Christensen, N.I., 1997. Seismic velocities of lower crustal and upper mantle rocks form the slow-spreading Mid-Atlantic Ridge, south of the Kane transform zone (MARK). Proceedings of the Ocean Drilling Program Science Results 153, 437–454.

Minshull, T.A., Muller, M.R., White, R.S., 2006. Crustal structure of the Southwest Indian Ridge at 66°E: seismic constraints. Geophysical Journal International 166, 135–147. https://doi.org/10.1111/j.1365-246X.2006.03001.x.

Muller, M.R., Minshull, T.A., White, R.S., 1999. Segmentation and melt supply at the Southwest Indian Ridge. Geology 27, 867. https://doi.org/10.1130/0091-7613(1999)027<0867:SAMSAT>2.3.CO;2.

Neal, C., Stanger, G., 1983. Hydrogen generation from mantle source rocks in Oman. Earth and Planetary Science Letters 66, 315–320. https://doi.org/10.1016/0012-821X(83)90144-9.

Normand, C., Williams-Jones, A.E., Martin, R.F., Vali, H., 2002. Hydrothermal alteration of olivine in a flow-through autoclave: Nucleation and growth of serpentine phases. American Mineralogist 87, 1699–1709.

Oufi, O., Cannat, M., Horen, H., 2002. Magnetic properties of variably serpentinized abyssal peridotites. Journal of Geophysical Research 107.

Padrón-Navarta, J.A., Sánchez-Vizcaí, V.L., Garrido, C.J., Gómez-Pugnaire, M.T., 2011. Metamorphic record of high-pressure dehydration of antigorite serpentinite to chlorite harzburgite in a subduction setting (Cerro del Almirez, Nevado-Filábride complex, Southern Spain). Journal of Petrology 52, 2047–2078. https://doi.org/10.1093/petrology/egr039.

Palandri, J.L., Reed, M.H., 2004. Geochemical models of metasomatism in ultramafic systems: serpentinization, rodingitization, and sea floor carbonate chimney precipitation. Geochimica et Cosmochimica Acta 68, 1115–1133. https://doi.org/10.1016/j.gca.2003.08.006.

Patriat, P., Sloan, H., Sauter, D., 2008. From slow to ultraslow: a previously undetected event at the Southwest Indian Ridge at ca. 24 Ma. Geology 36, 207–210. https://doi.org/10.1130/G24270A.1.

Paulick, H., Bach, W., Godard, M., De Hoog, J.C.M., Suhr, G., Harvey, J., 2006. Geochemistry of abyssal peridotites (Mid-Atlantic Ridge, 15°20′N, ODP Leg 209): Implications for fluid/rock interaction in slow spreading environments. Chemical Geology 234, 179–210. https://doi.org/10.1016/j.chemgeo.2006.04.011.

Plümper, O., Røyne, A., Magrasó, A., Jamtveit, B., 2012. The interface-scale mechanism of reaction-induced fracturing during serpentinization. Geology 40, 1103–1106. https://doi.org/10.1130/G33390.1.

Rouméjon, S., Cannat, M., 2014. Serpentinization of mantle-derived peridotites at mid-ocean ridges: Mesh texture development in the context of tectonic exhumation. Geochemistry, Geophysics and Geosystems 15, 2354–2379. https://doi.org/10.1002/2013GC005148.

Rouméjon, S., Cannat, M., Agrinier, P., Godard, M., Andreani, M., 2015. Serpentinization and Fluid Pathways in Tectonically Exhumed Peridotites from the Southwest Indian Ridge (62-65 E). Journal of Petrology 56, 703–734. https://doi.org/10.1093/petrology/egv014.

Rouméjon, S., Früh-Green, G.L., Orcutt, B.N., the IODP Expedition 357 Science Party, 2018. Alteration heterogeneities in peridotites exhumed on the southern wall of the Atlantis Massif (IODP Expedition 357). Journal of Petrology https://doi.org/10.1093/petrology/egy065.

Saccocia, P.J., Seewald, J.S., Shanks, W.C., 1998. Hydrogen and Oxygen Isotope Fractionation between Brucite and Aqueous NaCl Solutions from 250 to 450°C. Geochimica et Cosmochimica Acta 62, 485–492.

Saccocia, P.J., Seewald, J.S., Shanks, W.C., 2009. Oxygen and hydrogen isotope fractionation in serpentine–water and talc–water systems from 250 to 450°C, 50MPa. Geochimica et Cosmochimica Acta 73, 6789–6804. https://doi.org/10.1016/j.gca.2009.07.036.

Sauter, D., Cannat, M., Meyzen, C., Bezos, A., Patriat, P., Humler, E., Debayle, E., 2009. Propagation of a melting anomaly along the ultraslow Southwest Indian Ridge between 46°E and 52°20′E: interaction with the Crozet hotspot? Geophysical Journal International 179, 687–699. https://doi.org/10.1111/j.1365-246X.2009.04308.x.

Sauter, D., Cannat, M., Rouméjon, S., Andreani, M., Birot, D., Bronner, A., Brunelli, D., Carlut, J., Delacour, A., Guyader, V., MacLeod, C.J., Manatschal, G., Mendel, V., Ménez, B., Pasini, V., Ruellan, E., Searle, R.C., 2013. Continuous exhumation of mantle-derived rocks at the Southwest Indian Ridge for 11 million years. Nature Geoscience 6, 314–320. https://doi.org/10.1038/ngeo1771.

Schwartz, S., Guillot, S., Reynard, B., Lafay, R., Debret, B., Nicollet, C., Lanari, P., Auzende, A. L., 2013. Pressure-temperature estimates of the lizardite/antigorite transition in high pressure serpentinites. Lithos 178, 197–210. https://doi.org/10.1016/j.lithos.2012.11.023.

Scicchitano, M.R., Rubatto, D., Hermann, J., Shen, T., Padrón-Navarta, J.A., Williams, I.S., Zheng, Y.-F., 2018. In situ oxygen isotope determination in Serpentine minerals by ion microprobe: reference materials and applications to ultrahigh-pressure Serpentinites. Geostandards and Geoanalytical Research https://doi.org/10.1111/ggr.12232.

Seyfried, W.E., Foustoukos, D.I., Fu, Q., 2007. Redox evolution and mass transfer during serpentinization: an experimental and theoretical study at 200°C, 500bar with implications for ultramafic-hosted hydrothermal systems at Mid-Ocean Ridges. Geochimica et Cosmochimica Acta 71, 3872–3886. https://doi.org/10.1016/j.gca.2007.05.015.

Shannon, R.D., 1976. Revised Effective Ionic Radii and Systematic Studies of Interatomic Distances in Halides and Chalcogenides. Acta Crystallographica 32, 751–767.

Shock, E.L., Sassani, D.C., Willis, M., Sverjensky, D.A., 1997. Inorganic species in geologic fluids: Correlations among standard molal thermodynamic properties of aqueous ions and hydroxide complexes. Geochimica et Cosmochimica Acta 61, 907–950. https://doi.org/10.1016/S0016-7037(96)00339-0.

Sverjensky, D.A., Harrison, B., Azzolini, D., 2014. Water in the deep Earth: the dielectric constant and the solubilities of quartz and corundum to 60 kb and 1200 C. Geochimica et Cosmochimica Acta 129, 125–145.

Taylor, H.P.J., 1977. Water/rock interactions and the origin of in granitic batholiths. Journal of the Geological Society of London 133, 509–558.

Tutolo, B.M., Mildner, D.F.R., Gagnon, C.V.L., Saar, M.O., Seyfried, W.E., 2016. Nanoscale constraints on porosity generation and fluid flow during serpentinization. Geology 44. https://doi.org/10.1130/G37349.1.

Viti, C., Mellini, M., 1998. Mesh textures and bastites in the Elba retrograde serpentinites. European Journal of Mineralogy 10, 1341–1359.

Wegner, W.W., Ernst, W.G., 1983. Experimentally determined hydration and dehydration reaction rates in the system MgO-SiO2-H2O. American Journal of Science 283, 151–180.

Wenner, D.B., Taylor, H.P.J., 1971. Temperatures of Serpentinization of Uhramafic Rocks based on O18/O16 Fractionation between Coexisting Serpentine and Magnetite. Contribution Mineral Petrology 32, 165–185.

Wicks, F.J., Whittaker, E.J.W., 1977. Serpentine textures and serpentinization. The Canadian Mineralogist 15, 459–488.

Zervas, C.E., Sempéré, J.-C., Lin, J., 1995. Morphology and crustal structure of a small transform fault along the Mid-Atlantic Ridge: the Atlantis Fracture Zone. Marine Geophysical Researches 17, 275–300. https://doi.org/10.1007/BF01203466.

Zheng, Y.-F., 1993. Calculation of oxygen isotope fractionation in hydroxyl-bearing silicates. Earth and Planetary Science Letters 120, 247–263. https://doi.org/10.1016/0012-821X(93)90243-3.